

Autonomous quantum error correction and fault-tolerant quantum computation with squeezed cat qubits

Qian Xu,^{1,*} Guo Zheng,^{1,*} Yu-Xin Wang,¹ Peter Zoller,^{2,3} Aashish A. Clerk,¹ and Liang Jiang^{1,†}

¹*Pritzker School of Molecular Engineering, The University of Chicago, Chicago 60637, USA*

²*Institute for Theoretical Physics, University of Innsbruck, Innsbruck A-6020, Austria*

³*Institute for Quantum Optics and Quantum Information of the Austrian Academy of Sciences, Innsbruck A-6020, Austria*

(Dated: October 25, 2022)

We propose an autonomous quantum error correction scheme using squeezed cat (SC) code against the dominant error source, excitation loss, in continuous-variable systems. Through reservoir engineering, we show that a structured dissipation can stabilize a two-component SC while autonomously correcting the errors. The implementation of such dissipation only requires low-order nonlinear couplings among three bosonic modes or between a bosonic mode and a qutrit. While our proposed scheme is device independent, it is readily implementable with current experimental platforms such as superconducting circuits and trapped-ion systems. Compared to the stabilized cat, the stabilized SC has a much lower dominant error rate and a significantly enhanced noise bias. Furthermore, the bias-preserving operations for the SC have much lower error rates. In combination, the stabilized SC leads to substantially better logical performance when concatenating with an outer discrete-variable code. The surface-SC scheme achieves more than one order of magnitude increase in the threshold ratio between the loss rate κ_1 and the engineered dissipation rate κ_2 . Under a practical noise ratio $\kappa_1/\kappa_2 = 10^{-3}$, the repetition-SC scheme can reach a 10^{-15} logical error rate even with a small mean excitation number of 4, which already suffices for practically useful quantum algorithms.

I. INTRODUCTION

Quantum information is fragile to errors introduced by the environment. Quantum error correction (QEC) protects quantum systems by correcting the errors and removing the entropy [1–3]. Based upon QEC, fault-tolerant quantum computation (FTQC) can be performed, provided that the physical noise strength is below an accuracy threshold [4–7]. However, realizing FTQC is yet challenging due to the demanding threshold requirement and the significant resource overhead [8–11]. Unlike discrete-variable (DV) systems, continuous-variable (CV) systems possess an infinite-dimensional Hilbert space. Encoding the quantum information in CV systems, therefore, provides a hardware-efficient approach to QEC [12–16]. Various bosonic codes have been experimentally demonstrated to suppress errors in CV systems [17–22].

The standard QEC procedure relies on actively measuring the error syndromes and performing feedback control [1]. However, such adaptive protocols demand fast, high-fidelity coherent operations and measurements, which poses significant experimental challenges. At this stage, the error rates in the encoded level are still higher than the physical error rates in current devices due to the errors during the QEC operations [23–26]. To address these challenges, we may implement QEC non-adaptively via engineered dissipation – an approach called autonomous QEC (AutoQEC) [27]. Such an approach avoids the measurement imperfection and overhead associated with the classical feedback loops. Autonomous QEC in bosonic systems that can magnificently

suppress the dephasing noise has been demonstrated using the two-component cat code [20, 22, 28]. However, AutoQEC against excitation loss, which is usually the dominant error source in a bosonic mode, remains challenging. It requires either large nonlinearities that are challenging to engineer (e.g., the multiphoton processes needed for the multi-component cat codes [29]) or couplings to an intrinsically nonlinear DV system [30, 31] that is much noisier than the bosonic mode.

In this work, we propose an AutoQEC scheme against excitation loss with low-order nonlinearities and accessible experimental resources. Our scheme is, in principle, device-independent and readily implementable in superconducting circuits and trapped-ion systems. The scheme is based on the squeezed cat (SC) encoding, which involves the superposition of squeezed coherent state. We introduce an explicit AutoQEC scheme for the SC against loss errors by engineering a nontrivial dissipation, which simultaneously stabilizes the SC states and corrects the loss errors. We show that the engineered dissipation is close to the optimal recovery obtained using a semidefinite programming [32–34]. Notably, our proposed dissipation can be implemented with the same order of nonlinearity as that required by the two-component cat, which has been experimentally demonstrated in superconducting circuits [20] and shown to be feasible in trapped-ion systems [35].

Furthermore, we show that similar to the stabilized cat qubits, the stabilized SC qubits also possess a biased noise channel (with one type of error dominant over others), with an even larger bias (defined to be the ratio between the dominant error rate and the others) $\sim e^{\bar{n}^2}$ (compared to $\sim e^{\bar{n}}$ for the cat), where \bar{n} denotes the mean excitation number of the codewords. Consequently, we can concatenate the stabilized SC qubits with a DV code

* These authors contributed equally.

† liang.jiang@uchicago.edu

tailored towards the biased noise to realize low-overhead fault tolerant QEC and quantum computation [36–41]. We develop a set of operations for the SC that are compatible with the engineered dissipation and can preserve the noise bias needed for the concatenation. Compared to those for the cat [42], these operations suffer less from the loss errors because of the AutoQEC. Moreover, they can be implemented faster due to a larger dissipation gap and a cancellation of the leading-order non-adiabatic errors. In combination, the access to higher-quality operations leads to much better logical performance in the concatenated level using the SC qubits. For instance, we can achieve one-to-two orders of magnitude improvement in the κ_1/κ_2 threshold, where κ_1 is the excitation loss rate and κ_2 is the engineered dissipation rate, for the surface-SC and repetition-SC scheme (compared to surface-cat and repetition-cat, respectively). Furthermore, the repetition-SC can easily achieve a logical error rate as low as 10^{-15} , which already suffices for many useful quantum algorithms [8, 43], even using a small SC with $\bar{n} = 4$ under a practical noise ratio $\kappa_1/\kappa_2 = 10^{-3}$.

We note that aspects of the SC encoding were also recently studied in Ref. [44], with an emphasis on the enhanced protection against dephasing provided by squeezing (a point already noted in Refs. [45–47]). Unlike our work, Ref. [44] neither explored the enhanced noise bias provided by squeezing, nor exploited the ability to concatenate the SC code with outer DV codes using bias-preserving operations; as we have discussed, these are key advantages of the SC approach. Our work also goes beyond Ref. [44] in providing an explicit, fully autonomous approach to SC QEC that exploits low-order nonlinearities, and it is compatible with several experimental platforms. In contrast, Ref. [44] studied an approach requiring explicit syndrome measurements and a formal, numerically-optimized recovery operation. It was unclear how such an operation could be feasibly implemented in experiment. We also note that the SC has also been studied in the context of quantum transduction [48] (a very different setting than that considered here).

II. RESULTS

Squeezed cat encoding

The codewords of the SC are defined by applying a squeezing along the displacement axis (which is taken to be real) to the cat codewords:

$$|SC_{r,\alpha'}^\pm\rangle := \hat{S}(r)|C_{\alpha'}^\pm\rangle \quad (1)$$

where $|C_{\alpha'}^\pm\rangle := \mathcal{N}_\pm(|\alpha'\rangle + |-\alpha'\rangle)$ with $\mathcal{N}_\pm = \frac{1}{\sqrt{2(1 \pm e^{-2\alpha'^2})}}$ being normalization factors, and $\hat{S}(r) := \exp[\frac{1}{2}r(\hat{a}^2 - \hat{a}^{\dagger 2})]$ is the squeezing operator. The above codewords with even ($|SC_{r,\alpha'}^+\rangle$) and odd ($|SC_{r,\alpha'}^-\rangle$) excitation number parity are defined to be the X-basis eigenstates. The performance of the code is related to the

mean excitation number \bar{n} of its codewords. For a code with fixed \bar{n} , the amplitude α' of the underlying coherent states varies with the squeezing parameter r as

$$\alpha' \approx \sqrt{\bar{n} - \sinh^2 r} e^r, \quad (2)$$

which holds for the regime of interest where $\alpha' > 1$. Note that α' is closely related to how separated in phase space the two computational-basis states are, which determines their resilience against local error processes. At fixed \bar{n} , α'^2 can be written as a concave quadratic function of e^{2r} , which has a maximum $\alpha'_{\max}^2 = \bar{n}^2 + \bar{n}$.

For the SC, it is convenient to consider the subsystem decomposition of the oscillator Hilbert space $\mathcal{H} = \mathcal{H}_L \otimes \mathcal{H}_g$, where \mathcal{H}_L represents a logical sector of dimension 2 (which we refer to as a logical qubit) and \mathcal{H}_g represents a gauge sector of infinite dimension (which we refer to as a gauge mode). Analogous to the modular subsystem decomposition of the GKP qubit [49], whose logical sector carries the modular value of the quadratures, the logical sector of the SC carries the parity information (excitation number modulo 2). We can choose a basis under the subsystem decomposition spanned by squeezed displaced Fock states $|\pm\rangle_L \otimes |\hat{n} = n\rangle_g \approx \mathcal{N}_{\pm,n} \hat{S}(r)[\hat{D}(\alpha') \pm (-1)^n \hat{D}(-\alpha')]|n\rangle$ (we use \approx since the right-hand side should be orthonormalized within each parity branch. See supplement. [50] for details). By choosing this basis, the SC codewords in Eq. (1) coincide with $|\pm\rangle_L \otimes |\hat{n} = 0\rangle_g$, i.e., the codespace is the two-dimensional subspace obtained by projecting the gauge mode to the ground state. Furthermore, the bosonic annihilation operator \hat{a} can be expressed as

$$\hat{a} = \hat{Z}_L \otimes (e^{-r}\alpha' + \cosh r\hat{a} - \sinh r\hat{a}^\dagger) + \mathcal{O}(e^{-2\alpha'^2}), \quad (3)$$

where \hat{Z}_L is the Pauli Z operator acting on the logical qubit, and $\hat{a} = \sum_{n=0}^{\infty} \sqrt{n+1}|\hat{n} = n\rangle_g \langle \hat{n} = n+1|$ is the annihilation operator acting on the gauge mode.

Typical bosonic systems suffer from excitation loss (\hat{a}), heating (\hat{a}^\dagger), and dephasing ($\hat{a}^\dagger\hat{a}$) errors, with loss being the prominent one. To understand why the SC code can correct excitation loss errors, we consider the Knill–Laflamme conditions [51, 52] and evaluate the QEC matrices for loss errors [16]. Consider a pure loss channel with a loss probability γ , the leading-order Kraus operators are $\{\hat{I}, \sqrt{\gamma}\hat{a}\}$. The detectability of a single excitation loss is quantified by the matrix:

$$\begin{aligned} \hat{P}_{\text{code}}\hat{a}\hat{P}_{\text{code}} &= e^{-r}\alpha' \frac{q+q^{-1}}{2} \hat{Z}_c + ie^r\alpha' \frac{q-q^{-1}}{2} \hat{Y}_c \\ &\approx \sqrt{\bar{n} - \sinh^2 r} \hat{Z}_c - ie^r\alpha' e^{-2\alpha'^2} \hat{Y}_c, \end{aligned} \quad (4)$$

where \hat{P}_{code} is the projection onto the code space, \hat{Z}_c (\hat{Y}_c) is the Pauli Z (Y) operator in the code space and $q := \sqrt{\frac{1-e^{-2\alpha'^2}}{1+e^{-2\alpha'^2}}}$. The approximation in the second line is made in the regime of interest where $\alpha' \gg 1$. Eq. (4) indicates that a single excitation loss mostly

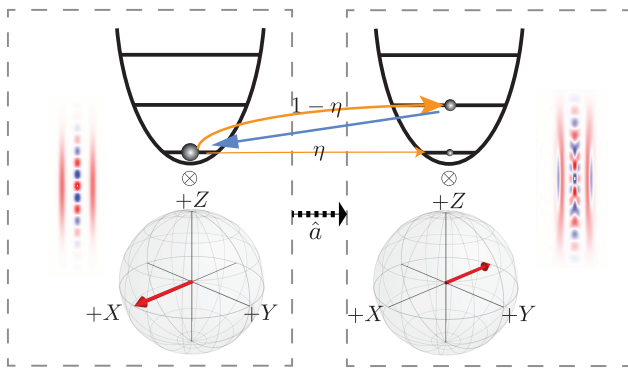


FIG. 1. The illustration of a SC that suffers from a single excitation loss and then approximately corrects it. Each dashed box represents a state (visualized by the Wigner function) of the SC, which is decomposed as a product of a logical qubit and a gauge mode. A single excitation loss corrupts the codeword $|+\rangle_c$ (left) into the state $\hat{a}|+\rangle_c/\sqrt{\langle +|_c\hat{a}^\dagger\hat{a}|+\rangle_c}$ (right). During such a process, a phase flip happens on the logical qubit, and a fraction $1 - \eta$ of the gauge mode population gets excited (indicated by the thick orange arrow). The excited population can be detected and then corrected, as indicated by the blue arrow.

leads to undetectable logical phase-flip errors, and the undetectability decreases with the squeezing parameter r . The increase of the detectability of single excitation loss events with the squeezing r can be better understood by considering the action of the decomposed \hat{a} operator (Eq. (3)) on the codeword $\hat{a}(|+\rangle_L \otimes |0'\rangle_g) = |-\rangle_L \otimes \sqrt{\bar{n}}(\sqrt{\eta}|0'\rangle - \sqrt{1-\eta}|1'\rangle)$, where

$$\eta := (\bar{n} - \sinh^2 r)/\bar{n}. \quad (5)$$

As shown in Fig. 1, after a single excitation loss, the branch of the population (with ratio η) that stays in the ground state of the gauge mode leads to undetectable logical phase-flip errors. In contrast, the other branch (with ratio $1 - \eta$) that goes to the first excited gauge state is in principle detectable. The detectable branch is also approximately correctable since $\hat{P}_{\text{code}}\hat{a}^\dagger\hat{a}\hat{P}_{\text{code}} \approx \bar{n}\hat{I}_c + \mathcal{O}(e^{-2\alpha'^2})\hat{X}_c$. Therefore, we expect that we can suppress the loss-induced phase flip errors by a factor η that decreases with the squeezing r . Moreover, the \hat{X}_c and \hat{Y}_c terms in the QEC matrices for both loss, heating, and dephasing are exponentially suppressed by α'^2 . As shown in Eq. (2), α'^2 can be greatly increased by adding squeezing (with $\alpha'_{\text{max}}^2 = \bar{n}^2 + \bar{n}$). Consequently, we expect that the SC can also have significantly enhanced noise bias compared to the cat.

Autonomous quantum error correction

While we have shown that the SC encoding can, in principle, detect and correct the loss errors, it remains a non-trivial task to find an explicit and practical recovery channel. In this section, we provide such a recovery channel, showing surprisingly that it requires only experimental resources that have been previously demon-

strated. As shown by the blue arrow in Fig. 1, we can, in principle, perform photon counting measurement on a probe field that is weakly coupled to the gauge mode, and apply a feedback parity flip \hat{Z}_L on the logical qubit upon detecting an excitation in the probe field [53]. Such measurement and feedback process can be equivalently implemented by applying the dissipator:

$$\hat{F} = (\hat{Z}_L \otimes \hat{I})\hat{S}(r)(\hat{a}^2 - \alpha'^2)\hat{S}^\dagger(r). \quad (6)$$

When $\alpha' \gg 1$, $\hat{F} \propto \hat{Z}_L \otimes \hat{a}$ represents a logical phase flip conditioned on the gauge mode losing an excitation. In the Fock basis, such an operator can be approximately given by

$$\hat{F} \approx \frac{e^r}{\alpha'}(c_1\hat{a} + c_2\hat{a}^\dagger)\hat{S}(r)(\hat{a}^2 - \alpha'^2)\hat{S}^\dagger(r), \quad (7)$$

with $c_1 + c_2 = 1$. In Methods, we propose two reservoir-engineering approaches to implement such a nontrivial dissipator using currently accessible experimental resources. We sketch the main ideas here. The first approach utilizes three bosonic modes that are nonlinearly coupled. As shown in Fig. 5(a), a high-quality mode b and a lossy mode c , together, serve as a non-reciprocal bath that provides a directional interaction $e^{-i\theta\hat{Z}_L} \otimes \hat{a}$ from the gauge mode to the logical qubit in the storage mode a . Such a coupled system can be physically realized in, e.g., superconducting circuits [20, 54]. The second approach couples a bosonic mode nonlinearly to a qutrit $\{|g\rangle, |e\rangle, |f\rangle\}$. As shown in Fig. 6, the bosonic mode is coupled to the gf transition via $\hat{S}(r)(\hat{a}^2 - \alpha'^2)\hat{S}^\dagger(r)|f\rangle\langle g| + h.c.$ and to the ef transition via $\hat{Z}_L|e\rangle\langle f| + h.c.$. By enhancing the decay from $|e\rangle$ to $|g\rangle$, we can obtain the effective dissipator \hat{F} by adiabatically eliminating both $|e\rangle$ and $|f\rangle$. Such a system can be physically realized in, e.g., trapped-ion system [35].

With the engineered dissipator in Eq. (6), the SC can be autonomously protected from excitation loss, heating and dephasing. The dynamics of the system are described by the Lindblad master equation:

$$\begin{aligned} \frac{d\hat{\rho}}{dt} &= \kappa_2\mathcal{D}[\hat{F}]\hat{\rho} + \kappa_1(1 + n_{\text{th}})\mathcal{D}[\hat{a}]\hat{\rho} \\ &+ \kappa_1n_{\text{th}}\mathcal{D}[\hat{a}^\dagger]\hat{\rho} + \kappa_\phi\mathcal{D}[\hat{a}^\dagger\hat{a}]\hat{\rho}, \end{aligned} \quad (8)$$

where $\mathcal{D}[\hat{A}]\hat{\rho} := \hat{A}\hat{\rho}\hat{A}^\dagger - \frac{1}{2}\{\hat{A}^\dagger\hat{A}, \hat{\rho}\}$. The logical phase-flip and bit-flip error rates of the SC under the dynamics described by Eq. (8) can be analytically obtained (see Methods for the derivations):

$$\gamma_Z = [\kappa_1(1 + 2n_{\text{th}}) + \kappa_\phi e^{-2r}](\bar{n} - \sinh^2 r), \quad (9)$$

$$\gamma_{X,Y} = \kappa_\phi \frac{(\bar{n} - \sinh^2 r)e^{2r}(\sinh^2 2r/4 + \cosh 4r)}{2\sinh(2(\bar{n} - \sinh^2 r)e^{2r})}, \quad (10)$$

where $\gamma_{X,Y}$ denotes the sum of the logical X and Y error rates, which we refer to as the bit-flip rate for simplicity [55]. We only consider the dephasing for $\gamma_{X,Y}$ since the loss-induced bit-flip rate has a more favorable scaling $\sim e^{-4\alpha'^2}$ with α' [54, 56]. The loss and the heating

contribute to γ_Z in the same way (both suppressed by a factor η) since their undetectable portion (η) is the same (see Eq. (3) and its hermitian conjugate). The dephasing also contributes to γ_Z , but with an extra e^{-2r} suppression, when combined with the parity-flipping dissipator \hat{F} . See Methods for details. Setting $r = 0$ and removing the κ_ϕ term in γ_Z , we restore the error rates of the dissipative cat [42].

In the regime where $e^{-r} \ll 1$ and γ_Z is mainly contributed by excitation loss, we can simplify Eqs. (9) and (10) as

$$\gamma_Z \approx \eta \bar{n} \kappa_1, \gamma_{X,Y} \approx \frac{9}{16} \kappa_\phi \alpha'^2 e^{-2\alpha'^2} e^{4r}, \quad (11)$$

where

$$\alpha' \approx \sqrt{4\eta(1-\eta)\bar{n}}. \quad (12)$$

As plotted in Fig. 2(a), fixing \bar{n} , γ_Z decreases monotonically with the squeezing r (unless r approaches the maximum squeezing $r_{\max} \approx \sinh^{-1}(\sqrt{\bar{n}})$. See Methods for details) as the undetectable portion η of the loss-induced errors decreases (see Eq. (5)). The change of $\gamma_{X,Y}$ with r (or equivalently, η) is roughly captured by the change in the displacement amplitude α' (see Eq. (12)), and $\gamma_{X,Y}$ takes the minima roughly when α' reaches the maxima $\alpha'_{\max} = \sqrt{\bar{n}^2 + \bar{n}}$. Note that the minimal bit-flip rate of the SC enjoys a more favorable scaling $\gamma_{X,Y} \propto e^{-2\bar{n}^2}$ with \bar{n} , compared to $\gamma_{X,Y} \propto e^{-2\bar{n}}$ for the cat, so that the SC can have a much larger noise bias under the same excitation number constraint. In principle, one needs to consider the tradeoff between γ_Z and α' and choose the optimal η depending on the tasks of interest. Smaller η leads to better protection from excitation losses, which is preferred by, e.g., the idling operations. Larger α' , on the other hand, leads to a larger noise bias and a widened dissipation gap [57] ($\propto \alpha'^2$), which can support faster operations, e.g., the bias-preserving CX gate introduced in the next section. In the following, we fix $\bar{n} = 4$ and $\eta = 1/4$ if not specified otherwise, which corresponds to a squeezing of $r = 1.32$ (11.5 dB). Such a parameter choice leads to $\gamma_Z \approx \kappa_1$, which removes the enhancement factor \bar{n} present for the cat (for $\bar{n} = 4$). Meanwhile, $\alpha'^2 \approx \frac{3}{4}\bar{n}^2$ provides a sufficiently large noise bias and dissipation gap.

In Fig. 2(b), we benchmark the performance of our Auto-QEC scheme against loss errors by comparing it to the optimal recovery channel given by a semidefinite programming (SDP) method [32–34]. We consider the joint channel $\mathcal{N} = \mathcal{D} \cdot \mathcal{N}_\gamma \cdot \mathcal{E}$, where \mathcal{E} denotes the encoding map from a qubit to the SC, \mathcal{N}_γ denotes a Gaussian pure loss channel (corresponding to Eq. (8) with $\kappa_2 = \kappa_\phi = n_{\text{th}} = 0$) with loss probability $\gamma := \kappa_1 t$, and \mathcal{D} denotes the recovery channel either using the autonomous QEC with the dissipator Eq. (6) or the optimal recovery channel. We evaluate the entanglement infidelity (EI) $1 - F_e$, where F_e denotes the entanglement fidelity, of the joint channel \mathcal{N} , as a function of the loss

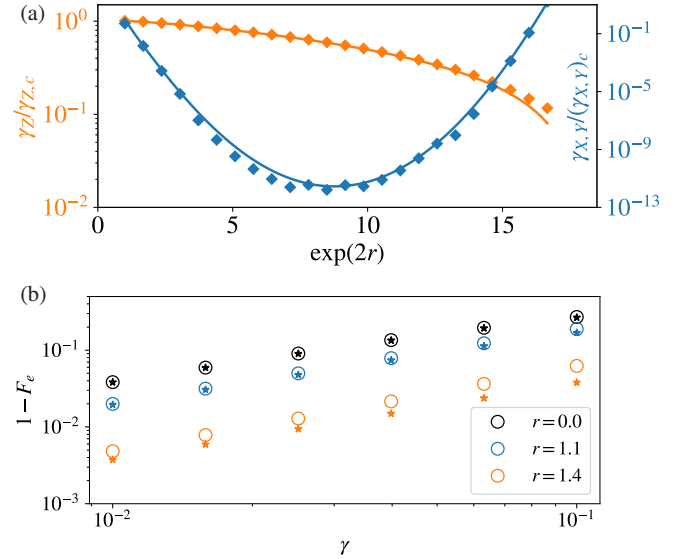


FIG. 2. (a) The phase γ_Z (orange) and bit $\gamma_{X,Y}$ (cyan) error rate of the dissipatively stabilized SC as a function of squeezing r under the parameters $\bar{n} = 4, \kappa_1 = 100\kappa_\phi = \kappa_2/100, n_{\text{th}} = 0.01$. The solid lines represent the analytical expressions Eqs. (9) and (10) while the diamonds represent the numerically extracted values. All the error rates are normalized by those of the dissipative cat $\gamma_{Z,c}, (\gamma_{X,Y})_c$, which are given by Eqs. (9) and (10) with $r = 0$. (b) The entanglement infidelity of a joint loss and recovery channel varying with the loss probability γ for the SC encoding with $\bar{n} = 4$. The recovery channel is either the engineered dissipation (the circles) or the optimal recovery channel determined by an SDP program [32–34] (the stars).

probability γ . Note that the EI is the objective function for the SDP. As shown in Fig. 2(b), the EI obtained using the Auto-QEC is close to the optimal EI, especially in the low- γ regime, demonstrating that our proposed autonomous QEC scheme is close to optimal for correcting excitation loss errors. We note that it is crucial to have the phase-flip \hat{Z}_L correction in the dissipator \hat{F} in order to correct the loss-induced phase-flip errors. Otherwise, a simple dissipator $\hat{S}(r)(\hat{a}^2 - \alpha'^2)\hat{S}^\dagger(r)$ directly generalized from the dissipative cat would still give an unsuppressed phase-flip rate $\gamma_Z = \kappa_1 \bar{n}$.

We note that the SC encoding also emerges as the optimal or close-to-optimal single-mode bosonic code through a bi-convex optimization (alternating SDP) procedure for a loss and dephasing channel with dephasing being dominant, as shown in Ref. [58].

Bias-preserving operations

To apply the autonomously protected SC for computational tasks, we need to develop a set of gate operations that are compatible with the engineered dissipation. Furthermore, the operations should preserve the biased noise channel of the SC, which can be utilized for resource-efficient concatenated QEC and fault-tolerant quantum computing [40, 41, 54, 59, 60]. Following the literature for the cat and the pair-cat [42,

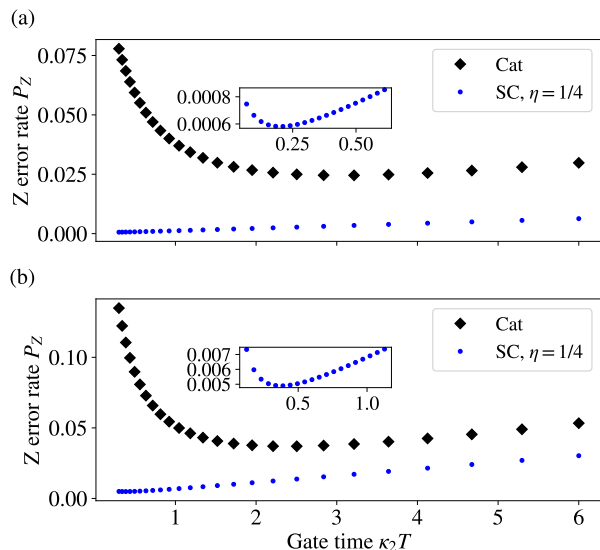


FIG. 3. The total Z error probability of the $Z(\pi)$ gates (a) and the CX gates (b) as a function of the gate time. For the CX gate, $p_Z := p_{Z_c} + p_{Z_t} + p_{Z_c Z_t}$ is the sum of the control-mode, target-mode, and the correlated phase flip rates. κ_1/κ_2 is fixed at 10^{-3} . The blue lines represent the gates on the cat qubits [42], and the red lines represent our proposed gates on the SC qubits with $\eta = 1/4$. \bar{n} is chosen as 4 for both cat and SC. The insets are the zoomed-in error rates of the SC gates around the optimal gate times.

[61–63], we develop a set of bias-preserving operations $\mathcal{B} = \{\mathcal{P}_{|\pm\rangle_c}, \mathcal{M}_X, X, Z(\theta), ZZ(\theta), \text{CNOT}, \text{Toffoli}\}$ for the SC, which suffice for many concatenated QEC schemes (e.g. concatenation with the repetition codes or the surface codes). The detailed design of each operation is presented in Methods.

Overall, the bias-preserving operations for the SC can achieve much higher fidelity (lower dominant Z -type error rates) than those for the cat for the following two reasons: (1). The operations suffer less from the excitation loss errors, which are (partially) autonomously corrected. (2). The non-adiabatic errors are significantly suppressed by the \hat{Z}_L correction in the dissipator \hat{F} (see Eq. (6)) and the enlarged dissipation gap ($\propto \alpha'^2$), so that the gate operations could be implemented faster. In Fig. 3, we show the total Z -type error rates for the Z -axis rotation $Z(\theta)$ and the CX gate as a function of the gate time. Compared to the cat gates in Ref. [42] with the same \bar{n} , the SC $Z(\theta)$ (CX) gate can achieve a 42.0 (7.56) times reduction in the lowest error rates. While we have fixed $\eta = 1/4$ as mentioned in last section, it is not necessarily the optimal choice of the squeezing. In fact, with η approaching $1/2$, we obtain even lower errors at faster gate times.

We note that compared to the cat stabilized by $\hat{a}^2 - \alpha^2$ in the literature, a simple extension to a SC stabilized by $\hat{S}(r)(\hat{a}^2 - \alpha'^2)\hat{S}^\dagger(r)$ can also lead to improvement in the gate speed and fidelities due to the enlarged dissipa-

tion gaps. However, adding the extra phase flip in the dissipator brings a much more significant improvement due to the suppression of the loss-induced errors and the leading-order non-adiabatic errors. See Discussion for more details.

Concatenated quantum error correction

With the bias-preserving operations, we can concatenate the SC with an outer discrete-variable code to suppress the logical error rates to the desired level. To compare the SC with the standard cat, we follow the literature and consider the concatenation with a repetition code [42] and a thin rotated surface code [54]. The surface-cat scheme can arbitrarily suppress the errors in a resource-efficient manner once the ratio between the loss rate κ_2 and the engineered dissipation rate κ_1 is below a certain threshold. The repetition-cat, on the other hand, cannot arbitrarily suppress the errors for a cat with constrained \bar{n} . Below a κ_1/κ_2 threshold, as the repetition code size increases, the logical Z error rate is exponentially suppressed while the logical X error is linearly amplified. Thus, a minimal total logical error rate is present. The concatenated QEC schemes with the cat are yet challenging since the κ_1/κ_2 thresholds (e.g., $\sim 5 \times 10^{-4}$ for the surface-cat, see Fig. 4(a)) are very demanding because of the low-fidelity bias-preserving operations. Also, the minimal logical error probability of the repetition-cat (e.g., $\sim 10^{-5}$ for $\bar{n} = 8$, see Fig. 4(d)) is still too high for fault-tolerant algorithms even using a relatively large cat because of the limited noise bias. In this section, we show that the κ_1/κ_2 thresholds for both the surface code and the repetition code can be significantly improved by concatenating with the dissipative SC. Moreover, the repetition-SC can reach sufficiently low logical error probability $\sim 10^{-15}$ even using a small SC $\bar{n} = 4$ (see Fig. 4(d)).

We first consider the concatenation of the SC with a d_X by d_Z thin surface code. Similar to Ref. [54], we fix the X distance d_X to 3, which suffices to suppress the logical X error rate, and increase the Z distance d_Z to suppress the logical Z error rate. At fixed $\eta = 1/4$, we obtain the logical Z error probability for d_Z code cycles as a function of κ_1/κ_2 for different d_Z , as shown in Fig. 4(a). The physical error rates of each physical operation involved in the surface-code QEC are presented in supplement [50]. We obtain a κ_1/κ_2 threshold at 0.93%, which is around 20 times higher than that of the surface-cat [54]. Note that by optimizing over the choice of the squeezing, the maximum threshold we obtained for $\bar{n} = 4$ is around 1.2%. Moreover, in Fig. 4(b) we show that this threshold can be further increased to about 3% by increasing \bar{n} to 7. Note that the κ_1/κ_2 threshold of the surface-cat remains the same when increasing \bar{n} . We attribute the increase of the κ_1/κ_2 threshold (for the concatenated SC schemes) to the reduced physical-operation error rates (see the previous section).

Next we consider the concatenation of the SC with a repetition code with size d_Z . As shown in Fig. 4(c), we obtain a 3.9% κ_1/κ_2 threshold for the logical Z error rate

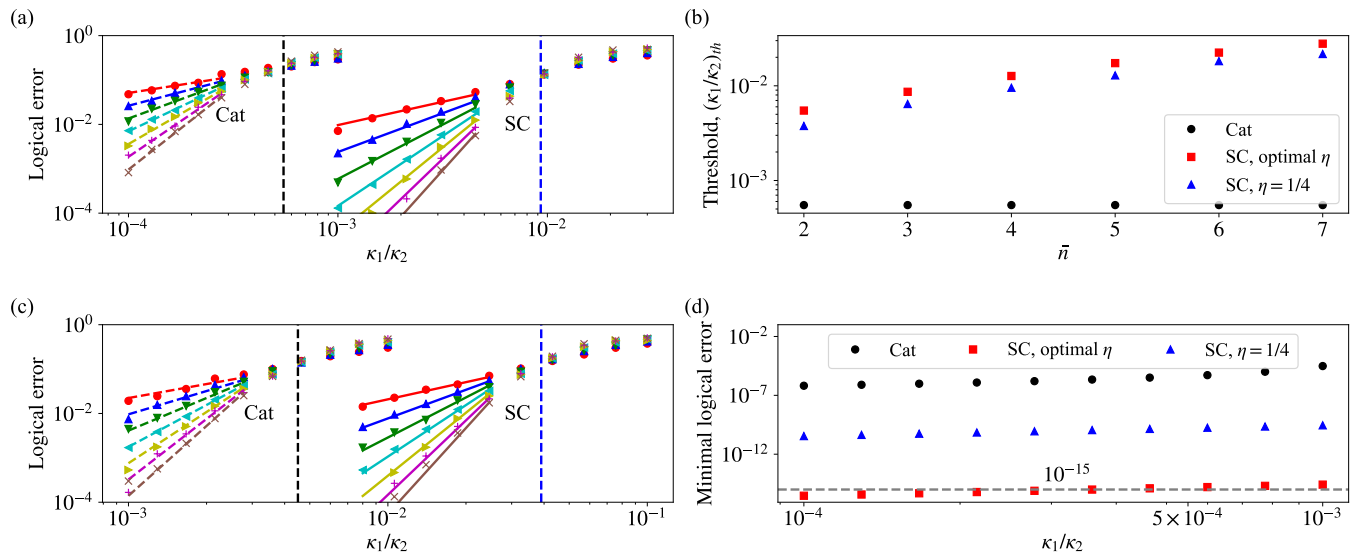


FIG. 4. Logical errors of the SC and the cat concatenated with repetition codes or surface codes. (a) Surface code logical Z error probabilities for a range of code distance $d_Z = 3, 5, 7, \dots, 15$ (from red to brown) with fixed $d_X = 3$. The SC is fixed to $\bar{n} = 4, \eta = 1/4$. The dashed lines indicate the threshold values of κ_1/κ_2 . (b) Surface code thresholds in κ_1/κ_2 varying with the average excitation number of the SC or the cat. (c) Repetition code logical Z error probabilities for a range of code size d_Z . (d) Repetition code minimum total logical error probabilities at $\kappa_1/\kappa_2 = 10^{-4}$, under the long gate time constraint $T \geq 1/\kappa_2$. The cat we consider has an average excitation number $\bar{n} = 8$. The logical error probabilities for both the surface codes and the repetition codes are obtained from Monte Carlo simulations of d_Z code cycles and one final round of perfect stabilizer measurement. We use the same minimum-weight-perfect-matching (MWPM) decoder as described in Ref. [54]

(again, see supplement [50] for the physical error rates used for the simulation), which is roughly 9 times higher than that of the repetition-cat. Below the κ_1/κ_2 threshold, as previously mentioned, a minimal total logical error rate is present. To obtain the minimal total logical error rate (by optimizing over d_Z), we find approximate expressions for the logical Z and X error probabilities in the sub-threshold regime ($\kappa_1/\kappa_2 < 10^{-3}$):

$$\begin{aligned} p_L^Z &\approx 0.059d_Z \left(\frac{p'_Z}{0.056} \right)^{0.48d_Z}, \\ p_L^X &\approx 2d_Z(d_Z - 1)p_{X,Y}, \end{aligned} \quad (13)$$

where $p'_Z := p_{Z_t} + p_{Z_c Z_t}$ denotes the sum of the target-mode and the correlated phase-flip rate of the CX gate (phase flips on the control mode have negligible contribution to the logical error rate for the repetition code), $p_{X,Y}$ the total non- Z error rates of the CX gate (the total rates of all the two-qubit Pauli errors that do not contain Z terms). p'_Z and $p_{X,Y}$ are in general functions of the CX gate time $\kappa_2 T$. To obtain simple expressions for them, we restrict the CX gate time to be $\kappa_2 T \geq 1$. In this regime, we have $p'_Z \approx \kappa_1 \bar{n} T$, $p_{X,Y} \approx 5.57 \times \frac{e^{-2\alpha'^2}}{\alpha'^2} \frac{1}{\kappa_2 T}$.

In Fig. 4(d), we plot the minimal total logical error probability $p_L = p_L^Z + p_L^X$ of the repetition-SC by optimizing d_Z and $\kappa_2 T$ for $\bar{n} = 4$ and $\eta = 1/4$. As a comparison, we also included minimal logical error probabilities of the repetition-cat with $\bar{n} = 8$ using the physical error rates in Ref. [54]. For a practical noise ratio $\kappa_1/\kappa_2 = 10^{-3}$, the

minimal logical error probability of the repetition-SC can reach $\sim 10^{-15}$, which suffices for many useful quantum computational tasks [8, 43]. In contrast, the logical error probability of the repetition-cat can only reach $\sim 10^{-5}$, which is far from being useful. To reach a similar level of logical error probability as the repetition-SC, we need either a much larger cat with $\bar{n} \gg 10$ (with the repetition code), or a more sophisticated outer code, e.g., the surface code. We attribute the drastic reduction in the minimal logical error rate of the repetition-SC, compared to the repetition-cat, to the significantly enhanced noise bias (or equivalently, the reduced physical bit-flip rates) of the SC.

III. DISCUSSION

Additional comparisons with the cat

Although in this work we benchmark the performance of the concatenated codes as a function of κ_1/κ_2 for both the cat and the SC, it might be of different difficulty level to engineer the same dissipation rate κ_2 for the cat and the SC, depending on the hardware implementation. Therefore, we can compare the performance of the concatenated codes as a function of κ_1/M , where M is the physical rate that is most challenging to engineer in practice. Here we focus on the implementation in superconducting circuits.

For example, stabilizing a cat with $\bar{n}_c = \alpha^2$ requires

the nonlinear coupling $g_2(\hat{a}^2 - \alpha^2)\hat{c}^\dagger + h.c.$ between the cat and a lossy mode c with a loss rate κ_c . The adiabatic elimination condition requires that $2\alpha g_2 \ll \kappa_c$, which can be satisfied by setting $2\alpha g_2 = \epsilon \kappa_c$ where $\epsilon \ll 1$ is a constant. Then κ_2 is proportional to κ_c : $\kappa_2 = \frac{4g_2^2}{\kappa_c} = \epsilon^2 \frac{\kappa_c}{\alpha^2}$. If the major hardware challenge is to engineer large κ_c [64], we can benchmark the performance of the concatenated codes as a function of κ_1/κ_c . For the SC, we have $\kappa_2 = \epsilon^2 \frac{\kappa_c}{\alpha^2}$. Using these relations between κ_2 and κ_c , we can compare the κ_1/κ_c thresholds instead of κ_1/κ_2 in Fig. 4(a). The κ_1/κ_c threshold of the surface-SC is still 12 times that of the surface cat.

Another potential hardware challenge is to engineer strong nonlinear couplings. In this case, we can compare the concatenated codes as a function of κ_1/J_{\max} , where J_{\max} denotes the largest nonlinear coupling strength required. For the cat, J_{\max} is simply given by g_2 and $\kappa_2 = \frac{2\epsilon J_{\max}}{\alpha}$. For the SC, since the challenging nonlinear coupling is in the form (see Eq. (16) in Methods) $J\hat{S}(r)(\hat{a}^2 - \alpha'^2)\hat{S}(r)^\dagger = J[\cosh^2 r \hat{a}^2 + \sinh^2 r \hat{a}^\dagger + \sinh r \cosh r \hat{a}^\dagger \hat{a} + \sinh r \cosh r - \alpha'^2]\hat{c}^\dagger + h.c.$, the largest coupling strength is $J_m = J \cosh^2 r = \frac{\alpha' \cosh^2 r \kappa_2}{2\epsilon}$. Using these relations, we can change the horizontal axis in Fig. 4(a) to κ_1/J_m and obtain about a 7 times increase in the κ_1/J_m threshold for the surface-SC compared to the surface-cat.

Comparison with the squeezed cat stabilized by a parity-preserving dissipator

To better understand the novelty and necessity of the parity-flipping dissipator \hat{F} we introduced in Eq. (6), we compare it with a parity-preserving dissipator

$$\hat{F}' = \hat{S}(r)(\hat{a}^2 - \alpha'^2)\hat{S}(r) \approx 2\alpha' \hat{I}_L \otimes \hat{a}, \quad (14)$$

which is a straightforward extension from $\hat{a}^2 - \alpha^2$ that stabilizes the cat. We show that the extra phase-flip correction in \hat{F} is essential for reducing SC's error rate in both the memory level and gate operations, which then leads to better logical performance in the concatenated level.

In the memory level, the change of a parity flip on the dissipator does not affect the bit-flip error rate we derived in Eq. (10). Nevertheless, \hat{F}' lacks the parity flip Z_L that corrects the detectable portion of the loss-induced errors, as shown clearly from Fig. 1 (the missing of the blue arrow). Therefore, a SC stabilized by \hat{F}' is not capable of correcting the loss errors. As such, it suffers from the same phase-flip error rate as a cat, $\gamma_Z = \kappa_1 \bar{n}$.

Regarding the gate operations, we take the Z rotation and the CNOT gate as examples. For the Z rotation, a SC stabilized by \hat{F}' only enjoys a suppression in the non-adiabatic errors by the increased adiabatic gap, $4\kappa_2 \alpha'^2$, compared to conventional cat of the same \bar{n} . In contrast, a SC stabilized by \hat{F} corrects the leading-order non-adiabatic error in $1/\alpha'^2$, since the extra \hat{Z}_L in \hat{F} compensates the parity-flip associated with the non-adiabatic transition (to the leading order). The residual errors are proportion to the correction factor, $\xi \propto 1/\alpha'^2$,

as discussed in Methods (see Eq. (30)). Therefore, while the minimal $Z(\theta)$ gate error for the SC with \hat{F}' is roughly suppressed by a factor $1/\bar{n}$ compared to the cat, that for the SC with \hat{F} is suppressed by an $1/\bar{n}^2$ factor (see Table I).

Normalized gate error	SC with \hat{F}'	SC with \hat{F}
$Z(\theta)$	$1/(\bar{n} + 1)$	$\sim \bar{n}^{-2}$
CNOT	$2/\sqrt{\bar{n} + 1}$	$\sim \bar{n}^{-3/2}$

TABLE I. Optimal gate error rate of the SC gates compared to the cat. All errors are normalized by the optimal gate errors of the cat, which are given by $p_{Z(\theta)} = \frac{\theta}{2} \sqrt{\frac{1}{\bar{n}} \frac{\kappa_1}{\kappa_2}}$ and $p_{\text{CNOT}} = \frac{\pi}{2\sqrt{2}} \sqrt{\frac{\kappa_1}{\kappa_2}}$ [54]. The definitions of \hat{F} and \hat{F}' are given in Eq. (6) and Eq. (14) respectively. The gate errors are optimized over both gate time and the squeezing for SC. Since the cooling time is mostly assumed to be constant in our gate scheme, it is neglected for simplicity. We only provide the scaling of the gate errors with \bar{n} for the SC since the exact expressions are complicated, as shown in Methods.

The errors of CNOT operation can be analyzed in a similar fashion. Due to the enlarged adiabatic gap, the minimal Z error rate of our SC gate with \hat{F}' is a factor of $\frac{2}{\sqrt{\bar{n}+1}}$ smaller than that of the cat gate [42]. For the mean excitation number we consider, $\bar{n} = 4$, this factor is only slightly less than 1. However, with the parity-flipping dissipator \hat{F} , the gate error enjoys a η suppression in the loss errors and an additional $\propto 1/\alpha'^2$ suppression in the non-adiabatic error. Combining these advantages, the CNOT gate error ratio with that of the cat roughly scales as $\bar{n}^{-3/2}$ (see Table I).

Since the fault-tolerant threshold is mostly limited by errors of the CNOT and the idling operation, the thresholds of the concatenated SC schemes using \hat{F}' is comparable to that of the concatenated cat scheme even at optimal squeezing for small mean excitation number. As such, having the extra phase-flip correction in the dissipator \hat{F} is crucial for concatenated QEC and fault-tolerant quantum computing.

Applications in superconducting circuits and trapped-ion systems

The stabilized cat qubits have been considered as a candidate for hardware-efficient, fault-tolerant, and scalable computation tasks in superconducting circuits [54, 60]. The dissipative SC, which we show has an overall advantage over the cat, could play an important role along this direction.

The dissipative SC could also find its application in trapped-ion systems. On the one hand, encoding into the motional states of the ions provides an alternative approach for storing and protecting the quantum information. How to process the information (e.g., implementing quantum gates) remains to be explored. On the other hand, if the information is stored in the internal states of the ions (the conventional approach), the bosonic codes like the SC could lead to more robust information pro-

cessing. One could utilize multi-species ions [65, 66] with multiple levels [67] and dissipatively protect the motional modes while leaving a subset of the ions' internal states that carry the information intact. The protected motional modes can, for instance, be used for scalable, parallel, and high-quality entangling gates mediated by localized phonon modes [68].

IV. METHODS

Physical realization of the dissipator

In this section, we present the details of the two approaches implementing the dissipator in Eq. (6). Before describing our recipes, it is worth discussing the challenges involved here. The most straightforward method to realizing a generic Lindblad dissipator $\mathcal{D}[\hat{F}]$ is to couple the system to an auxiliary reservoir mode c (with decay rate κ_c) via a coupling Hamiltonian $g(\hat{F}\hat{c}^\dagger + h.c.)$. In the limit where mode c acts as a Markovian environment for the system, i.e. $\kappa_c \gg g$, we realize the target dissipator \hat{F} with an effective dissipation rate $4g^2/\kappa_c$. For the dissipator in Eq. (6), this simple route requires a strong fourth-order nonlinear coupling, which has not been demonstrated yet due to the experimental challenges.

Here we present two approaches for realizing the desired nonlinear dissipator using accessible experimental resources: The first approach utilizes three nonlinearly-coupled bosonic modes, which can be physically realized in, e.g., superconducting circuits [20, 54]; The second approach couples a bosonic mode nonlinearly to a qutrit, which can be physically realized in, e.g., trapped-ion system [35].

The first approach only requires third-order nonlinearities to implement our desired dissipator, making use of a more structured engineered dissipation proposed in Ref. [69]. Under the subsystem decomposition of the storage mode a encoding the SC, one can realize a general nonlinear dissipator of the form $\mathcal{D}[e^{-i\theta\hat{Z}_L} \otimes \hat{A}]$ (with an angle θ), by coupling a gauge-mode operator \hat{A} and an auxiliary mode b to the input and output ports of a directional waveguide, respectively, and introducing a dispersive interaction between an auxiliary mode b and the logical qubit: $\hat{H}_{\text{disp.}} = \frac{\lambda}{2}\hat{Z}_L\hat{b}^\dagger\hat{b}$. For the dissipator in Eq. (6), we choose $\hat{A} = \hat{a}$. The physical interactions (in the Fock basis) can be obtained from the mapping $\hat{a} \rightarrow \frac{1}{2\alpha'}\hat{S}(r)(\hat{a}^2 - \alpha'^2)\hat{S}^\dagger(r)$, and $\hat{Z}_L \rightarrow \frac{1}{2\alpha'}\hat{S}(r)(\hat{a} + \hat{a}^\dagger)\hat{S}^\dagger(r)$, which means that we need a nonlinear coupling between the storage mode a and the waveguide port. While it is challenging to directly achieve this using e.g. a physical circulator, the directional dynamics can be synthetically engineered by adding another reservoir mode c . The whole setup is illustrated in Fig. 5(a), whose dynamics is given by master

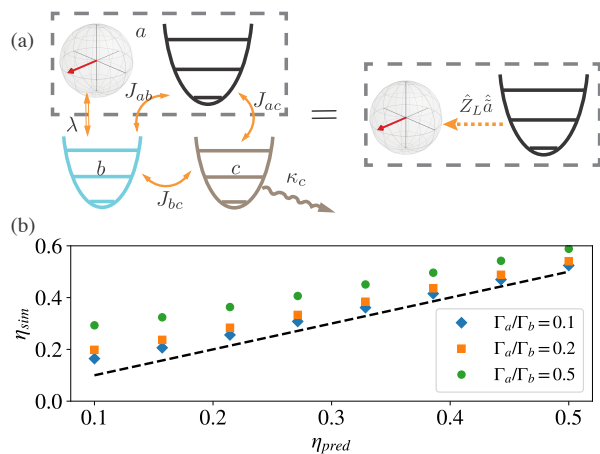


FIG. 5. (a) Realization of the parity-flipping dissipator $\hat{Z}_L \otimes \hat{a}$ using three nonlinearly coupled bosonic modes. (b) Comparison between the numerically extracted η (η_{sim}) and the theoretically predicted η (η_{pred} in Eq. (5)) for a range of finite Γ_a/Γ_b . The dashed line indicates the ideal case where $\eta_{\text{sim}} = \eta_{\text{pred}}$.

equation

$$\frac{d}{dt}\hat{\rho} = -i[\hat{H}_{\text{disp.}} + \hat{H}_{\text{tunn.}}, \hat{\rho}] + \kappa_c \mathcal{D}[\hat{c}], \quad (15)$$

where the tunnel coupling Hamiltonian $\hat{H}_{\text{tunn.}}$ of the total system-reservoir is given by

$$\hat{H}_{\text{tunn.}} = J_{ab}\hat{a}^\dagger\hat{b} + (J_{ac}\hat{a} - iJ_{bc}\hat{b})\hat{c}^\dagger + h.c., \quad (16)$$

$$J_{ab} = \sqrt{\Gamma_a\Gamma_b}/2, \quad J_{ac} = \sqrt{\Gamma_a\kappa_c}/2, \quad J_{bc} = \sqrt{\Gamma_b\kappa_c}/2. \quad (17)$$

In the regime where the joint b, c modes act as a Markovian reservoir for mode a , i.e. $\kappa_c \gg \sqrt{\Gamma_a\Gamma_b}$ and $\Gamma_b \gg \Gamma_a$, we can adiabatically eliminate both b and c to obtain an effective dissipator (using the effective operator formalism [70]), as

$$\frac{d}{dt}\hat{\rho} = \Gamma_a \mathcal{D} \left[\frac{i\lambda\hat{Z}_L - \Gamma_b\hat{a}}{i\lambda\hat{Z}_L + \Gamma_b} \hat{a} \right] \hat{\rho}. \quad (18)$$

Setting $\lambda = \Gamma_b$, we obtain the desired dissipator $\hat{Z}_L \otimes \hat{a}$ to stabilize the SC (see supplement. [50] for a detailed derivation).

Note that Eq. (16) still involves nonlinear couplings between the a, b and a, c modes. Fortunately, all the nonlinear terms are now cubic, which can be realized by parametrically pumping nonlinear elements (e.g., ATS [54], SNAIL [22]) that couples different modes with appropriate drive tones. We note that the nonlinearity required in Eq. (16) has been demonstrated for stabilizing a cat [20, 54].

When deriving Eq. (18), we require the physical setup Eq. (15) to operate in the regime where adiabatic elimination remains valid. It is thus natural to ask what are the imperfections given realistic physical parameters,

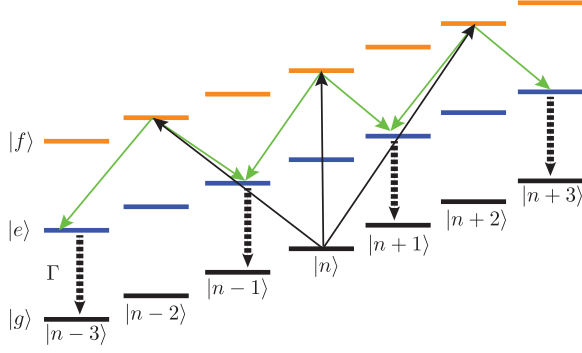


FIG. 6. Laser configuration for the coupling Hamiltonian in Eq. (20) for implementing the SC in trapped-ion system. The motional mode of the ion is coupled to three internal states via the sideband transitions, represented by the black and the green arrows. Starting from $|g\rangle \otimes |\psi\rangle$ ($|\psi\rangle$ is an arbitrary motional state), the system goes through a two-step coherent transition $|g\rangle \otimes |\psi\rangle \rightarrow |f\rangle \otimes \hat{F}_1|\psi\rangle \rightarrow |e\rangle \otimes \hat{F}_2\hat{F}_1|\psi\rangle$ (indicated by the black and the green solid arrows, respectively) and decays rapidly to $|g\rangle \otimes \hat{F}_2\hat{F}_1|\psi\rangle$ (indicated by the black dashed arrows). Here $\hat{F}_1 \propto \hat{S}(r)(\hat{a}^2 - \alpha'^2)\hat{S}^\dagger(r)$ and $\hat{F}_2 \propto \hat{S}(r)\hat{a}\hat{S}^\dagger(r)$. Adiabatically eliminating the $|e\rangle, |f\rangle$ states, we obtain the effective dissipator on the motional mode $\hat{F} = \hat{F}_2\hat{F}_1$.

i.e. when the decay rates κ_c, Γ_b of auxiliary modes b, c cannot be infinitely large. In that case, one can show the dominating error due to finite reservoir bandwidth is due to the finite decay rates κ_c and Γ_b , and it is preferable to set $\kappa_c \sim \Gamma_b$ to optimize over hardware resources (see supplement. [50] for details). In this regime, the extra error introduced by physical implementation is determined by the ratio Γ_a/Γ_b , which heuristically describes the branching ratio between the logical qubit population that does not undergo the parity flip (uncorrected error) and the population that does (corrected error) whenever a gauge mode excitation decays into the environment. More specifically, as shown in supplement [50], we can approximately derive the discrepancy between the desired suppression factor for the loss-induced phase flip rate η_{pred} (using Eq. (5)) and the numerically extracted (achievable) value η_{sim} , as $\eta_{\text{sim}} - \eta_{\text{pred}} = (1 - \eta_{\text{pred}})(\Gamma_a/2\Gamma_b)$. As shown in Fig. 5(b), by setting $\Gamma_a/\Gamma_b = 0.1$, we can realize the desired η within 50% accuracy.

Now we present the second approach for implementing the dissipator $\hat{F} = \frac{1}{\alpha'}\hat{S}(r)\hat{a}(\hat{a}^2 - \alpha'^2)\hat{S}^\dagger(r)$ using a coupled boson-qutrit system. Note that a simpler dissipator stabilizing a cat $\hat{a}^2 - \alpha^2$ was obtained using a coupled boson-qubit system in trapped-ion platform in Ref. [35]. However, the dissipator \hat{F} cannot be directly engineered using their approach since there are many frequency-degenerate terms, e.g., \hat{a} and $\hat{a}^\dagger\hat{a}^2$, that cannot be independently controlled by a single sideband drive. To resolve this, we generalize their approach by introducing a third internal level of the ion, and implementing the dissipator \hat{F} in two steps associated with different electronic transitions. Specifically, we use the motional mode

of the ions in a 1D harmonic trap as the bosonic mode, which is coupled to three internal levels $|g\rangle, |e\rangle$ and $|f\rangle$ via several laser beams:

$$\frac{d}{dt}\hat{\rho} = -i[\hat{H}_{\text{eff}}, \hat{\rho}] + \mathcal{J}\hat{\rho}, \quad (19)$$

where $\hat{H}_{\text{eff}} = \nu\hat{a}^\dagger\hat{a} + \omega_e|e\rangle\langle e| + \omega_f|f\rangle\langle f| + \frac{1}{2}\Omega_0(|f\rangle\langle g|e^{-i\omega_f t} + h.c.) + \hat{H}_{\text{coup}} - i\frac{\Gamma}{2}|e\rangle\langle e|$, with

$$\hat{H}_{\text{coup}} = \sum_{i=1}^3 \Omega_i \cos[\eta_0(\hat{a} + \hat{a}^\dagger)](|f\rangle\langle g|e^{-i(\omega_f + \delta_i)t} + h.c.) + \sum_{i=4}^5 \Omega_i \sin[\eta_0(\hat{a} + \hat{a}^\dagger)](|e\rangle\langle f|e^{-i(\omega_e - \omega_f + \delta_i)t} + h.c.), \quad (20)$$

and

$$\mathcal{J}\hat{\rho} = \Gamma \int_{-1}^1 du N(u) e^{-i\eta_0 u(\hat{a} + \hat{a}^\dagger)} \times |g\rangle\langle e|\hat{\rho}|e\rangle\langle g| e^{i\eta_0 u(\hat{a} + \hat{a}^\dagger)}. \quad (21)$$

Here ν is the trap frequency, η_0 the Lamb-Dick parameter, Γ the engineered decay rate from $|e\rangle$ to $|g\rangle$, and $N(u)$ the normalized dipole pattern. \hat{H}_{coup} describes the coupling between the motional mode and the internal states, illustrated in Fig. 6, and $\mathcal{J}\hat{\rho}$ describes the spontaneous emission of the ion from $|e\rangle$ to $|g\rangle$ and its associated momentum kicks. The drive with amplitude Ω_0 in \hat{H}_{eff} comes from a laser that is coupled to the ion along a constrained (transverse) direction, thereby only driving the internal transitions. By tuning the laser detunings $\delta_1 = -2\nu, \delta_2 = 2\nu, \delta_3 = 0, \delta_4 = -\nu$, and $\delta_5 = \nu$, and choosing appropriate driving strength $\{\Omega_i\}$ (see supplement. [50]), we can obtain a coupling Hamiltonian (neglecting the fast-rotating terms):

$$\hat{H}_{\text{coup}} = \Omega'_{gf}\hat{S}(r)(\hat{a}^2 - \alpha'^2)\hat{S}^\dagger(r)|f\rangle\langle g| + \Omega'_{ef}\frac{1}{\alpha'}\hat{S}(r)\hat{a}\hat{S}^\dagger(r)|e\rangle\langle f| + h.c. \quad (22)$$

In the regime where $2\alpha'\Omega'_{gf} \ll \Gamma, \Omega'_{gf} \ll \Omega'_{ef}$, we can obtain a reduced dynamics on the motional mode by adiabatically eliminating the $|e\rangle, |f\rangle$ states:

$$\frac{d}{dt}\hat{\rho}_m = \kappa_2\mathcal{D}[\hat{F}]\hat{\rho}_m, \quad (23)$$

where $\hat{\rho}_m$ is the reduced density matrix on the motional mode. Through numerical simulations we find that we can obtain the dissipator \hat{F} with the desired rate by setting $\Omega'_{ef} = 0.5\Gamma, \Omega'_{gf}/\Omega'_{ef} = 1/20$. A large κ_2 , therefore, demands large Γ and driving strength. Note that we have assumed that Γ and $\{\Omega_i\}, i = 1, 2, 3, 4, 5$ are much smaller than ν , so that the off-resonant terms can be safely neglected (secular approximation). In practice, however, one might be able to go beyond this weak-drive regime by carefully cancelling the effects from the off-resonant

terms. We have also neglected the effects from the momentum kicks here, which only lead to a small increase in the phase-flip suppression factor $\eta \rightarrow \eta + \mathcal{O}(\eta_0^2)$. See supplement. [50] for a more detailed analysis. We stress that our proposed approach requires the same order of nonlinearity as that required by a two-component cat, which has been considered to be feasible in trapped-ion system [35].

The memory error rates of the squeezed cat

In this section, we provide the derivation of the memory error rates for the SC in Eqs. (9) and (10).

Since the bit-flip error rate is exponentially small in α' , the subsystem decomposition is insufficient to obtain an analytical expression of it. Thus, we derive the bit-flip error rate using the conserved quantities of the system [29, 71]. To facilitate the analysis, we first neglect the \hat{Z}_L term in the dissipator in Eq. (6) since it does not contribute to the bit-flip rate, and then analyze the system dynamics in the squeezed frame:

$$\frac{d\hat{\rho}_s}{dt} = \kappa_2 \mathcal{D}[\hat{a}^2 - \alpha'^2] \hat{\rho}_s + \kappa_\phi \mathcal{D}[\hat{a}_s^\dagger \hat{a}_s] \hat{\rho}_s, \quad (24)$$

where $\hat{A}_s := \hat{S}^\dagger(r) \hat{A} \hat{S}(r)$ for any operator \hat{A} . Note that we consider the dephasing here, which is the dominant source for the bit-flip errors. The two conserved quantities associated with the dominant dissipator $\hat{a}^2 - \alpha'^2$ are

$$\begin{aligned} \hat{J}_{++} &= \sum_{n=0}^{\infty} |2n\rangle \langle 2n|, \\ \hat{J}_{+-} &= \sqrt{\frac{2\alpha'^2}{\sinh 2\alpha'^2}} \sum_{q=-\infty}^{\infty} \frac{(-1)^q}{2q+1} I_q(\alpha'^2) \hat{J}_{+-}^{(q)}, \end{aligned} \quad (25)$$

where $I_q(\cdot)$ is the modified Bessel function of the first kind, and $\hat{J}_{+-}^{(q)} = \frac{(\hat{a}^\dagger \hat{a} - 1)!!}{(\hat{a}^\dagger \hat{a} + 2q)!!} \hat{J}_{++} \hat{a}^{2q+1}$ for $q \geq 0$ and $\hat{J}_{+-}^{(q)} = \hat{J}_{++} \hat{a}^{\dagger 2q+1} \frac{(\hat{a}^\dagger \hat{a})!!}{(\hat{a}^\dagger \hat{a} + 2|q| - 1)!!}$ for $q < 0$. The steady state coherence of the system initialized in $\hat{\rho}(0)$ can be computed through $c_{++}(\infty) = \text{tr} \left\{ J_{++}^\dagger \rho(0) \right\}$ and $c_{+-}(\infty) = \text{tr} \left\{ J_{+-}^\dagger \rho(0) \right\}$. Thus, we compute the bit-flip rate perturbatively by considering the dephasing in the squeezed frame,

$$\gamma_{X,Y} = -\kappa_\phi \text{tr} \left\{ J_{+-}^\dagger \mathcal{D} \left[\hat{S}^\dagger(r) \hat{a}^\dagger \hat{a} \hat{S}(r) \right] |C_\alpha^+\rangle \langle C_\alpha^-| \right\}, \quad (26)$$

which is then simplified to Eq. (10).

The phase-flip error rate Eq. (9) can be easily derived by analyzing the errors under the subsystem decomposition. The loss and heating errors are in the form $\hat{a} \approx \hat{Z}_L \otimes (e^{-r} \alpha' + \cosh r \hat{a} - \sinh r \hat{a}^\dagger)$, $\hat{a}^\dagger \approx \hat{Z}_L \otimes (e^{-r} \alpha' + \cosh r \hat{a}^\dagger - \sinh r \hat{a})$. They both contribute to the phase-flip rate via the undetectable term $e^{-r} \alpha' \hat{Z}_L = \sqrt{\eta \bar{n}} \hat{Z}_L$ (the detectable part associated with the $\hat{Z}_L \otimes \hat{a}^\dagger$ term is approximately correctable by \hat{F}). The dephasing is in the

form $\hat{a}^\dagger \hat{a} \approx \hat{I}_L \otimes [e^{-2r} \alpha'^2 + e^{-2r} \alpha' (\hat{a} + \hat{a}^\dagger) + \cosh^2 r \hat{a}^\dagger \hat{a} + \sinh^2 r \hat{a} \hat{a}^\dagger - \cosh r \sinh r (\hat{a}^2 + \hat{a}^{\dagger 2})]$. It contributes to the phase-flip rate dominantly by the $e^{-2r} \alpha' \hat{I}_L \otimes \hat{a}^\dagger$ term, which creates an excitation in the gauge mode that is subsequently destroyed by \hat{F} with a residual phase flip. Therefore, the dephasing contributes to the phase-flip rate by $\kappa_\phi e^{-4r} \alpha'^2 = \kappa_\phi e^{-2r} \eta \bar{n}$.

Eq. (9) is valid in the regime where $\alpha' \gg 1$, which is violated when r approaches the maximum squeezing allowed by the energy constraint. We now provide a leading-order correction to the loss-induced phase flip rate in such a regime. We have assumed that the dissipator $\hat{F} = \hat{Z}_L (\hat{a}^2 - \alpha'^2) \approx \hat{Z}_L \otimes (\hat{a}^2 + 2\alpha' \hat{a})$ can perfectly correct the detectable part of the loss-(or heating-)induced errors by removing the excitation in the gauge mode while applying a phase-flip correction on the logical qubit. However, it is not a perfect correction because of the non-Hermitian part of the dynamics induced by $F^\dagger F \approx \hat{I}_L \otimes [\hat{a}^{\dagger 2} \hat{a}^2 + 2\alpha' (\hat{a}^{\dagger 2} \hat{a} + \hat{a}^\dagger \hat{a}^2) + 4\alpha'^2 \hat{a}^\dagger \hat{a}]$. The second term above further excites the gauge mode, which introduces additional non-negligible Z errors when $\alpha' \gg 1$ does not hold. Through analysis of a simplified 3-level system, we obtain a correction factor for the phase-flip rate in the form of

$$\xi = \frac{1}{2(1 + 3\alpha'^2)}, \quad (27)$$

which works well for $\alpha' \geq 1.5$. This factor represents that, if the qubit evolves from an initial state of $|\pm\rangle_L \otimes |\bar{n} = 1\rangle$ under the dissipator \hat{F} , a population of $1 - \xi$ would end up in $|\mp\rangle_L \otimes |\bar{n} = 0\rangle$ and ξ would be in $|\pm\rangle_L \otimes |\bar{n} = 0\rangle$ in steady state. Therefore, the phase-flip rate in Eq. (9) has an extra correction:

$$\gamma_Z \rightarrow \gamma_Z + \kappa_1 (1 + n_{\text{th}}) \bar{n} (1 - \eta) \xi + \kappa_1 n_{\text{th}} (1 - \eta') \xi - \kappa_\phi e^{-2r} \eta \xi, \quad (28)$$

where $\eta' = (\bar{n} - \cosh^2 r) / \bar{n}$, which approaches η in the large squeezing limit.

The correction factor's effect becomes significant as η approaches 0. In the limit of large \bar{n} and only considering the dominant loss error, the Z error rate has a minimum value $\gamma_{Z,\text{min}} \approx \frac{\sqrt{2}}{4} \kappa_1$. Worth noticing, this minimum rate is independent of \bar{n} . Therefore, the SC enjoys an exponential suppression of the bit-flip rate while maintaining a bounded phase-flip rate by increasing \bar{n} , which is drastically different from the cat code or its DV counterpart, the repetition code.

Bias-preserving operations for the squeezed cat

In this section, we present the detailed design and error analysis for the Z rotation $Z(\theta)$ and the CX gate for the SC, which are representatives of bias-preserving operations \mathcal{B} . See supplement. [50] for the rest of the operations in \mathcal{B} .

Similarly to the cat, the Z-axis rotation $Z(\theta)$ can be generated by a resonant linear drive $\hat{H}_Z = \frac{\theta}{4\alpha'^T} e^r (\hat{a} + \hat{a}^\dagger)$ in the presence of the engineered dissipation in Eq. (6) for a time T . In the subsystem basis, $H_Z \approx \frac{\theta}{4\alpha'^T} \hat{Z}_L \otimes$

$(2\alpha' + \hat{a} + \hat{a}^\dagger)$. The total phase flip error probability of the Z rotation is $p_Z = p_Z^{\text{NA}}(T) + \kappa_1 \eta \bar{n} T$, where the second term represents the loss-induced phase flips and the first term represents the non-adiabatic errors due to the non-adiabatic excitation $\hat{Z}_L \otimes \hat{a}^\dagger$ in \hat{H}_Z . We note that compared to the parity-preserving dissipator $\mathcal{D}[\hat{I}_L \otimes \hat{a}]$, which is used in the literature for the cat (by applying a driven two-photon dissipation), the parity-flipping dissipator \hat{F} in Eq. (6) can significantly reduce the non-adiabatic errors induced by $\hat{Z}_L \otimes \hat{a}^\dagger$. The reason is that the majority of the parity flips associated with the non-adiabatic transitions can be flipped back through the application of the dissipator. The remaining errors with a fraction ξ leads to the residual non-adiabatic error p_Z^{NA} proportional to ξ (see the previous Methods section). Under the adiabatic limit $\frac{\theta}{4\alpha'T} \ll 4\kappa_2\alpha'^2$, the system's evolution under the dissipator \hat{F} can be approximated by the dynamics of the density matrix $\hat{\rho}_{\text{trunc}}$ with a truncated 2-level gauge basis:

$$\kappa_2 \mathcal{D}[\hat{F}] \hat{\rho} \approx 4\kappa_2 \alpha'^2 ((1 - \xi) \mathcal{D}[\hat{Z}_L \otimes \hat{a}] + \xi \mathcal{D}[\hat{I}_L \otimes \hat{a}]) \hat{\rho}_{\text{trunc}}. \quad (29)$$

Performing first-order adiabatic elimination [70] on the gauge excited state results in an effective Z error rate $\frac{\xi \theta^2}{16\kappa_2 \alpha'^4 T}$. Notice that adiabatic elimination does not capture the higher-order errors and the result only holds under the adiabatic limit. A more accurate expression can be derived through solving the ordinary differential equations of the two level system. As a result, the modified non-adiabatic error has the form:

$$p_Z^{\text{NA}}(T) = \frac{\xi \theta^2}{16\kappa_2 \alpha'^4 T^2} (c_1 T + c_2 \frac{e^{-2\kappa_2 \alpha'^2 T} - 1}{2\kappa_2 \alpha'^2}). \quad (30)$$

Performing numerical fit, we obtain $c_1 = 1.5, c_2 = 1.8$.

The CX gate is implemented by applying the engineered dissipation only on the control mode and a Hamiltonian term that drives a phase rotation on the target mode conditioned on the states of the control mode:

$$\begin{aligned} \frac{d}{dt} \hat{\rho} &= \kappa_2 \mathcal{D}[\hat{F}_c] \hat{\rho} - i[\hat{H}_{\text{CX}}, \hat{\rho}], \\ \hat{H}_{\text{CX}} &= \frac{\pi}{4\alpha'T} [e^r (\hat{a}_c + \hat{a}_c^\dagger) - 2\alpha'] (\hat{a}_t^\dagger \hat{a}_t - \alpha'^2), \end{aligned} \quad (31)$$

where \hat{F}_c denotes the engineered dissipator in Eq. (6) on the control mode. The noise terms are not shown for simplicity. We note that compared to the standard CX gate on the cat [42, 54], we turn off the dissipation on the target mode during the gate to circumvent the need for high-order coupling terms between the two modes. Although the target mode temporarily loses the protection against the excitation loss, we can still implement a high-quality gate if the gate time is short enough and the leakage on the target mode can be subsequently returned to the code space without introducing too many errors. Similar strategy and insights have been made in Ref. [72]. To deal with the non-adiabatic transitions

on the target mode, which preserve the parity, we apply a parity-preserving dissipation $\kappa_2 \mathcal{D}[\hat{S}(r)(\hat{a}_t^2 - \alpha'^2)\hat{S}^\dagger(r)]$ on the target mode (while the control mode is, as always, protected by the parity-flipping dissipation) for a time T_{cool} . In our simulations, we fix the cooling time $T_{\text{cool}} = 8 \times \frac{1}{4\kappa_2 \alpha'^2}$ to ensure that the leakage is suppressed to below 0.5%. Using the Pauli-twirling approximation, the Z -type errors of the CX gate are

$$\begin{aligned} p_{Z_c} &= \kappa_1 \eta \bar{n} (T + T_{\text{cool}}) + p_Z^{\text{NA}}(T), \\ p_{Z_t} &= \kappa_1 \bar{n} \left(\frac{T}{2} + T_{\text{cool}} \right), \\ p_{Z_c Z_t} &= \frac{1}{2} \kappa_1 \bar{n} T, \end{aligned} \quad (32)$$

where p_{Z_c}, p_{Z_t} and $p_{Z_c Z_t}$ denote the Z error on the control, target mode and the correlated Z error, respectively. They sum to the total Z error probability $p_Z = \kappa_1 \bar{n} (1 + \eta) (T + T_{\text{cool}}) + p_Z^{\text{NA}}(T)$. Note that, unlike the Z rotation, the CX gate does not enjoy a full suppression of the loss-induced errors (by a factor η) due to the lack of the engineered dissipation on the target mode during the gate. The non-adiabatic error $p_Z^{\text{NA}}(T)$ on the control mode has a similar form as Eq. (30):

$$p_Z^{\text{NA}}(T) = \frac{\xi \pi^2}{16\kappa_2 \alpha'^2 T^2} \left(1.5T + 0.6 \frac{e^{-2\kappa_2 \alpha'^2 T} - 1}{2\kappa_2 \alpha'^2} \right) \quad (33)$$

We also present the non- Z error rate of the CX gate here. Note that the CX gate has a significantly larger non- Z error rate than all other bias-preserving operations in \mathcal{B} . As discussed numerically in Ref. [54], the non- Z error of a cat's CX gate scales approximately as $1.8 \frac{e^{-2\alpha'^2}}{\alpha'^2} \frac{1}{\kappa_2 T}$. For our CX gate on the SC, we find a similar expression

$$p_{X,Y} = 5.57 \frac{e^{-2\alpha'^2}}{\alpha'^2} \frac{1}{\kappa_2 T}, \quad (34)$$

in the regime where $\kappa_2 T > 1$. Note that for shorter gate time, we cannot find a simple expression for $p_{X,Y}$ and a numerical simulation of the gate has to be performed to determine $p_{X,Y}$.

ACKNOWLEDGMENTS

We thank Ramesh Bhandari, Yvonne Gao, Kyungjoo Noh for helpful discussions. We acknowledge support from the ARO (W911NF-18-1-0020, W911NF-18-1-0212, W911NF-19-1-0380), ARO MURI (W911NF-16-1-0349, W911NF-21-1-0325), AFOSR MURI (FA9550-19-1-0399, FA9550-21-1-0209), AFRL (FA8649-21-P-0781), DoE Q-NEXT, NSF (PHY-1748958, OMA-1936118, ERC-1941583, OMA-2137642), NTT Research, and the Packard Foundation (2020-71479).

- [1] M. A. Nielsen and I. L. Chuang, *Quantum Computation and Quantum Information: 10th Anniversary Edition* (Cambridge University Press, 2010).
- [2] *Quantum Error Correction* (Cambridge University Press, 2013).
- [3] D. Aharonov, M. Ben-Or, R. Impagliazzo, and N. Nisan, [arXiv preprint quant-ph/9611028](#) (1996).
- [4] D. Aharonov and M. Ben-Or, in *Proceedings of the twenty-ninth annual ACM symposium on Theory of computing* (1997) pp. 176–188.
- [5] A. Y. Kitaev, [Russian Mathematical Surveys](#) **52**, 1191 (1997).
- [6] E. Knill, R. Laflamme, and W. H. Zurek, [Proceedings of the Royal Society of London. Series A: Mathematical, Physical and Engineering Sciences](#) **454**, 365 (1998).
- [7] P. Aliferis, D. Gottesman, and J. Preskill, [arXiv preprint quant-ph/0504218](#) (2005).
- [8] A. G. Fowler, M. Mariantoni, J. M. Martinis, and A. N. Cleland, [Physical Review A](#) **86**, 032324 (2012).
- [9] D. Litinski, [Quantum](#) **3**, 128 (2019).
- [10] R. Chao, M. E. Beverland, N. Delfosse, and J. Haah, [Quantum](#) **4**, 352 (2020).
- [11] M. E. Beverland, A. Kubica, and K. M. Svore, [PRX Quantum](#) **2**, 020341 (2021).
- [12] D. Gottesman, A. Kitaev, and J. Preskill, [Physical Review A](#) **64**, 012310 (2001).
- [13] I. L. Chuang, D. W. Leung, and Y. Yamamoto, [Physical Review A](#) **56**, 1114 (1997).
- [14] M. H. Michael, M. Silveri, R. Brierley, V. V. Albert, J. Salmilehto, L. Jiang, and S. M. Girvin, [Physical Review X](#) **6**, 031006 (2016).
- [15] P. T. Cochrane, G. J. Milburn, and W. J. Munro, [Physical Review A](#) **59**, 2631 (1999).
- [16] V. V. Albert, K. Noh, K. Duivenvoorden, D. J. Young, R. Brierley, P. Reinhold, C. Vuillot, L. Li, C. Shen, S. Girvin, *et al.*, [Physical Review A](#) **97**, 032346 (2018).
- [17] N. Ofek, A. Petrenko, R. Heeres, P. Reinhold, Z. Leghtas, B. Vlastakis, Y. Liu, L. Frunzio, S. Girvin, L. Jiang, *et al.*, [Nature](#) **536**, 441 (2016).
- [18] L. Hu, Y. Ma, W. Cai, X. Mu, Y. Xu, W. Wang, Y. Wu, H. Wang, Y. P. Song, C. L. Zou, S. M. Girvin, L. M. Duan, and L. Sun, [Nature Physics](#) **15**, 503 (2019).
- [19] P. Campagne-Ibarcq, A. Eickbusch, S. Touzard, E. Zalts-Geller, N. E. Frattini, V. V. Sivak, P. Reinhold, S. Puri, S. Shankar, R. J. Schoelkopf, *et al.*, [Nature](#) **584**, 368 (2020).
- [20] R. Lescanne, M. Villiers, T. Peronin, A. Sarlette, M. Delbecq, B. Huard, T. Kontos, M. Mirrahimi, and Z. Leghtas, [Nature Physics](#) **16**, 509 (2020).
- [21] C. Flühmann, T. L. Nguyen, M. Marinelli, V. Negnevitsky, K. Mehta, and J. P. Home, [Nature](#) **566**, 513 (2019).
- [22] A. Grimm, N. E. Frattini, S. Puri, S. O. Mundhada, S. Touzard, M. Mirrahimi, S. M. Girvin, S. Shankar, and M. H. Devoret, [Nature](#) **584**, 205 (2020).
- [23] L. Egan, D. M. Debroy, C. Noel, A. Risinger, D. Zhu, D. Biswas, M. Newman, M. Li, K. R. Brown, M. Cetina, *et al.*, [Nature](#) **598**, 281 (2021).
- [24] Y. Zhao, Y. Ye, H.-L. Huang, Y. Zhang, D. Wu, H. Guan, Q. Zhu, Z. Wei, T. He, S. Cao, *et al.*, [Physical Review Letters](#) **129**, 030501 (2022).
- [25] C. Ryan-Anderson, N. Brown, M. Allman, B. Arkin, G. Asa-Attuah, C. Baldwin, J. Berg, J. Bohnet, S. Braxton, N. Burdick, *et al.*, [arXiv preprint arXiv:2208.01863](#) (2022).
- [26] R. Acharya, I. Aleiner, R. Allen, T. I. Andersen, M. Ansmann, F. Arute, K. Arya, A. Asfaw, J. Atalaya, R. Babush, *et al.*, [arXiv preprint arXiv:2207.06431](#) (2022).
- [27] J. Lebreuilly, K. Noh, C.-H. Wang, S. M. Girvin, and L. Jiang, [arXiv preprint arXiv:2103.05007](#) (2021).
- [28] C. Berdou, A. Murani, U. Reglade, W. Smith, M. Villiers, J. Palomo, M. Rosticher, A. Denis, P. Morfin, M. Delbecq, *et al.*, [arXiv preprint arXiv:2204.09128](#) (2022).
- [29] M. Mirrahimi, Z. Leghtas, V. V. Albert, S. Touzard, R. J. Schoelkopf, L. Jiang, and M. H. Devoret, [New Journal of Physics](#) **16**, 045014 (2014).
- [30] B. Royer, S. Singh, and S. Girvin, [Physical Review Letters](#) **125**, 260509 (2020).
- [31] J. M. Gertler, B. Baker, J. Li, S. Shirol, J. Koch, and C. Wang, [Nature](#) **590**, 243 (2021).
- [32] M. Reimpell and R. F. Werner, [Physical review letters](#) **94**, 080501 (2005).
- [33] A. S. Fletcher, P. W. Shor, and M. Z. Win, [Physical Review A](#) **75**, 012338 (2007).
- [34] K. Noh, V. V. Albert, and L. Jiang, [IEEE Transactions on Information Theory](#) **65**, 2563 (2018).
- [35] J. Poyatos, J. I. Cirac, and P. Zoller, [Physical review letters](#) **77**, 4728 (1996).
- [36] D. K. Tuckett, S. D. Bartlett, and S. T. Flammia, [Physical review letters](#) **120**, 050505 (2018).
- [37] D. K. Tuckett, A. S. Darmawan, C. T. Chubb, S. Bravyi, S. D. Bartlett, and S. T. Flammia, [Physical Review X](#) **9**, 041031 (2019).
- [38] D. K. Tuckett, S. D. Bartlett, S. T. Flammia, and B. J. Brown, [Physical review letters](#) **124**, 130501 (2020).
- [39] J. P. Bonilla Ataides, D. K. Tuckett, S. D. Bartlett, S. T. Flammia, and B. J. Brown, [Nature communications](#) **12**, 1 (2021).
- [40] J. Roffe, L. Z. Cohen, A. O. Quintavalle, D. Chandra, and E. T. Campbell, [arXiv preprint arXiv:2202.01702](#) (2022).
- [41] Q. Xu, N. Mannucci, A. Seif, A. Kubica, S. T. Flammia, and L. Jiang, [arXiv preprint arXiv:2203.16486](#) (2022).
- [42] J. Guillaud and M. Mirrahimi, [Physical Review X](#) **9**, 041053 (2019).
- [43] J. O’Gorman and E. T. Campbell, [Physical Review A](#) **95**, 032338 (2017).
- [44] D. S. Schlegel, F. Minganti, and V. Savona, [arXiv preprint arXiv:2201.02570](#) (2022).
- [45] R. Teh, P. Drummond, and M. Reid, [Physical Review Research](#) **2**, 043387 (2020).
- [46] H.-Y. Lo, D. Kienzler, L. de Clercq, M. Marinelli, V. Negnevitsky, B. C. Keitch, and J. P. Home, [Nature](#) **521**, 336 (2015).
- [47] H. Le Jeannic, A. Cavallès, K. Huang, R. Filip, and J. Laurat, [Physical Review Letters](#) **120**, 073603 (2018).
- [48] H.-K. Lau and A. A. Clerk, [npj Quantum Information](#) **5**, 1 (2019).
- [49] G. Pantaleoni, B. Q. Baragiola, and N. C. Menicucci, [Physical Review Letters](#) **125**, 040501 (2020).
- [50] *Supplementary Material*.
- [51] C. H. Bennett, D. P. DiVincenzo, J. A. Smolin, and W. K. Wootters, [Physical Review A](#) **54**, 3824 (1996).
- [52] E. Knill and R. Laflamme, [Physical Review A](#) **55**, 900

- (1997).
- [53] J. A. Gross, C. M. Caves, G. J. Milburn, and J. Combes, *Quantum Science and Technology* **3**, 024005 (2018).
- [54] C. Chamberland, K. Noh, P. Arrangoiz-Arriola, E. T. Campbell, C. T. Hann, J. Iverson, H. Putterman, T. C. Bohdanowicz, S. T. Flammia, A. Keller, *et al.*, *PRX Quantum* **3**, 010329 (2022).
- [55] Note that similar to the cat [61], the full error channel of the stabilized SC, which is analyzed in detail in supplement. [50], is not a Pauli error channel in general. For simplicity, we make the Pauli-twirling approximation only keeping the diagonal terms of the process matrix in the Pauli basis.
- [56] J. Guillaud and M. Mirrahimi, *Physical Review A* **103**, 042413 (2021).
- [57] The nonzero eigenvalue of the Lindbladian $\mathcal{D}[\hat{F}]$ with the smallest real part, which characterizes the rate of the population decaying into the steady-state manifold.
- [58] P. Leviant, Q. Xu, L. Jiang, and S. Rosenblum, *arXiv preprint arXiv:2205.00341* (2022).
- [59] J. P. Bonilla Ataides, D. K. Tuckett, S. D. Bartlett, S. T. Flammia, and B. J. Brown, *Nature communications* **12**, 1 (2021).
- [60] A. S. Darmawan, B. J. Brown, A. L. Grimsmo, D. K. Tuckett, and S. Puri, *PRX Quantum* **2**, 030345 (2021).
- [61] S. Puri, L. St-Jean, J. A. Gross, A. Grimm, N. E. Fratini, P. S. Iyer, A. Krishna, S. Touzard, L. Jiang, A. Blais, *et al.*, *Science advances* **6**, eaay5901 (2020).
- [62] Q. Xu, J. K. Iverson, F. G. Brandão, and L. Jiang, *Physical Review Research* **4**, 013082 (2022).
- [63] M. Yuan, Q. Xu, and L. Jiang, *arXiv preprint arXiv:2208.06913* (2022).
- [64] For instance, κ_c is limited by filter bandwidth in Ref. [54].
- [65] I. V. Inlek, C. Crocker, M. Lichtman, K. Sosnova, and C. Monroe, *Physical review letters* **118**, 250502 (2017).
- [66] C. Bruzewicz, R. McConnell, J. Stuart, J. Sage, and J. Chiaverini, *npj Quantum Information* **5**, 1 (2019).
- [67] M. Ringbauer, M. Meth, L. Postler, R. Stricker, R. Blatt, P. Schindler, and T. Monz, *Nature Physics* **18**, 1053 (2022).
- [68] T. Olsacher, L. Postler, P. Schindler, T. Monz, P. Zoller, and L. M. Sieberer, *PRX Quantum* **1**, 020316 (2020).
- [69] Y.-X. Wang, C. Wang, and A. A. Clerk, *arXiv preprint arXiv:2203.09392* (2022).
- [70] F. Reiter and A. S. Sørensen, *Physical Review A* **85**, 032111 (2012).
- [71] V. V. Albert, *arXiv preprint arXiv:1802.00010* (2018).
- [72] R. Gautier, A. Sarlette, and M. Mirrahimi, *PRX Quantum* **3**, 020339 (2022).

Supplementary Material for “Autonomous quantum error correction and fault-tolerant quantum computation with squeezed cat qubits”

Qian Xu,^{1,*} Guo Zheng,^{1,*} Yu-Xin Wang,¹ Peter Zoller,^{2,3} Aashish A. Clerk,¹ and Liang Jiang^{1,†}

¹*Pritzker School of Molecular Engineering, The University of Chicago, Chicago 60637, USA*

²*Institute for Theoretical Physics, University of Innsbruck, Innsbruck A-6020, Austria*

³*Institute for Quantum Optics and Quantum Information of the Austrian Academy of Sciences, Innsbruck A-6020, Austria*

I. SUBSYSTEM DECOMPOSITION OF THE SQUEEZED CAT

We can divide the Hilbert space of a bosonic mode $\mathcal{H}_{CV} = \text{span}\{|n\rangle, n = 0, 1, 2, \dots\}$ into two orthogonal subspaces:

$$\mathcal{H}_{CV} = \mathcal{H}_{\text{even}} \oplus \mathcal{H}_{\text{odd}},$$

where $\mathcal{H}_{\text{even}}$ (\mathcal{H}_{odd}) is the $+1$ (-1) eigenspace of the parity operator $\hat{\Pi} := e^{-i\hat{n}\pi}$. Since both $\mathcal{H}_{\text{even}}$ and \mathcal{H}_{odd} are isomorphic to \mathcal{H}_{CV} , we can decompose \mathcal{H}_{CV} into two subsystems:

$$\mathcal{H}_{CV} = \mathbb{C}_L^2 \otimes \mathcal{H}_g,$$

where \mathbb{C}_L^2 is a Hilbert space of dimension 2 (which we refer to as a qubit), and $\mathcal{H}_g \simeq \mathcal{H}_{CV}$ is a Hilbert space of infinite dimension (which we refer to as a gauge mode). Under this decomposition, $|+\rangle_L \otimes |\psi\rangle_g$ ($|-\rangle_L \otimes |\psi\rangle_g$) is an even-(odd-) parity state for any $|\psi\rangle_g \in \mathcal{H}_g$. The choice of the gauge mode basis is not unique. For instance, we can choose a basis for \mathcal{H}_g based on the modular decomposition [1] of the number operator: $|+\rangle_L \otimes |m\rangle_g := |0+2m\rangle$ ($|-\rangle_L \otimes |m\rangle_g := |1+2m\rangle$). For the squeezed cat (SC), it is convenient to work with another basis related to the squeezed coherent states. We first define a set of non-orthonormalized states $|\psi_{n,\pm}\rangle := \mathcal{N}_{n,\pm} \hat{S}(r) \left[\hat{D}(\alpha') \pm (-1)^n \hat{D}(-\alpha') \right] |n\rangle$, where $\mathcal{N}_{n,\pm}$ is the normalization factor. Note that states with different parity \pm are orthogonal with each other. We then apply the Gram-Schmidt orthonormalization procedure to the states within each parity branch (starting from $|\phi_{0,\pm}\rangle$ and then increasing n) to obtain a set of orthonormalized states $\{|\Phi_{n,\pm}\rangle\}$. Note that the states $|\Phi_{n,\pm}\rangle$ are equivalent to the shifted fock basis introduced in Ref. [2] by a global squeezing transformation. Finally, we define a subsystem basis as

$$|\pm\rangle_L \otimes |\tilde{n} = n\rangle_g := |\Phi_{n,\pm}\rangle. \quad (1)$$

The choice of this subsystem basis can describe the SC more efficiently than the fock basis since $|\pm\rangle_L \otimes |\tilde{n} = 0\rangle_g$ coincides with the SC codewords. Furthermore, the physical states of a stabilized SC usually evolve within a subspace with low excitation in the gauge mode. As such, we can apply a truncation to the gauge mode and perform the analysis within a truncated $2d$ -dimensional (with d being a small integer) subspace of \mathcal{H}_{CV} : $\text{span}\{|\pm\rangle_L \otimes |\tilde{n} = n\rangle_g, n = 0, 1, \dots, d-1\}$.

II. ERROR CHANNEL OF THE DISSIPATIVELY STABILIZED SQUEEZED CAT

In this section, we provide a more detailed analysis on the error channel of the dissipatively stabilized cat, which can be represented by the process matrix χ : $\mathcal{E}(\hat{\rho}) = \sum_{i,j \in \{I,X,Y,Z\}} \chi_{i,j} \hat{\sigma}_i \hat{\rho} \hat{\sigma}_j$. In Fig. S1, we numerically obtain the matrix χ for a SC with $\bar{n} = 4, r = 0.2$ stabilized by the parity-flipping dissipator $\hat{Z}_L \hat{S}(r) (\hat{a}^2 - \alpha'^2) \hat{S}^\dagger(r)$ under loss, heating and dephasing. Since χ has off-diagonal elements the channel is not exactly a Pauli error channel. It is generally in the form $\mathcal{E}(\hat{\rho}) = (\lambda_I \hat{I} + \lambda_X \hat{X}) \hat{\rho} (\lambda_I \hat{I} + \lambda_X \hat{X})^\dagger + (\lambda_Y \hat{Y} + \lambda_Z \hat{Z}) \hat{\rho} (\lambda_Y \hat{Y} + \lambda_Z \hat{Z})^\dagger$, with coherence between \hat{I}, \hat{X} and \hat{Y}, \hat{Z} . Note that the cat has the same form of error channel [3]. The Pauli error rates $\gamma_X, \gamma_Y, \gamma_Z$ that we use in the main text refer to the diagonal elements of χ , which implicitly assumes the Pauli-twirling approximation.

* These authors contributed equally.

† liang.jiang@uchicago.edu

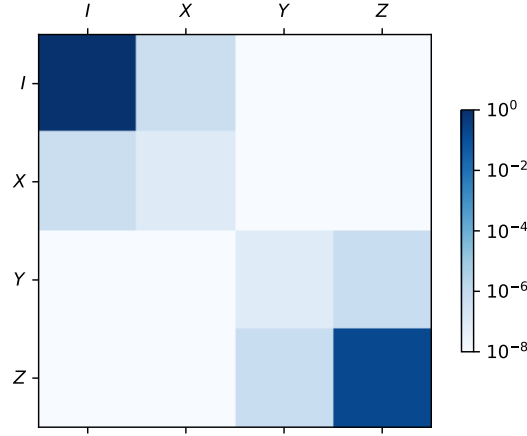


FIG. S1. The absolute value of the process matrix χ for a SC stabilized by $\kappa_2 \mathcal{D}[\hat{Z}_L \hat{S}(r)(\hat{a}^2 - \alpha'^2) \hat{S}^\dagger(r)]$ with $\bar{n} = 4, r = 0.2$ under $\kappa_1 = 10\kappa_\phi = \kappa_2/100, n_{\text{th}} = 0.02$ for a time $T = 5/\kappa_2$.

III. BIAS-PRESERVING OPERATIONS

In this section, we construct the remaining bias-preserving operations in $\mathcal{B} = \{\mathcal{P}_{|\pm\rangle_c}, \mathcal{M}_X, X, Z(\theta), ZZ(\theta), \text{CNOT}, \text{Toffoli}\}$, other than $Z(\theta)$ and CNOT presented in the main text.

The ZZ rotation can be implemented by applying the following beam-splitter Hamiltonian to two dissipatively stabilized modes: $\hat{H}_{ZZ} = \frac{\pi}{4\alpha'^2} e^{2r} (\hat{a}_1 \hat{a}_2^\dagger + \hat{a}_1^\dagger \hat{a}_2)$.

The Toffoli gate can be implemented similarly to the CX gate:

$$\begin{aligned} \frac{d}{dt} \hat{\rho} &= \kappa_2 \mathcal{D}[\hat{F}_{c_1}] + \kappa_2 \mathcal{D}[\hat{F}_{c_2}] - i[\hat{H}_{\text{Toff}}, \hat{\rho}], \\ \hat{H}_{\text{Toff}} &= -\frac{\pi}{8\alpha'^2 T} ((e^r \hat{a}_{c_1} - \alpha') (e^r \hat{a}_{c_2}^\dagger - \alpha') + \text{h.c.}) \times (\hat{a}_t^\dagger \hat{a}_t - \alpha'^2), \end{aligned}$$

where \hat{F}_{c_1} and \hat{F}_{c_2} are the parity-flipping dissipator on the c_1 and c_2 mode, respectively.

The X gate can be implemented by adiabatically tuning the phases of the stabilized code states $e^{-i\frac{\pi}{T} t \hat{a}^\dagger \hat{a}} |SC_{r,\alpha'}^\pm\rangle$ so that a π phase rotation is implemented in time T . By adding a counterdiabatic drive $\hat{H}_X = \frac{\pi}{T} \hat{a}^\dagger \hat{a}$ the non-adiabatic effects are completely suppressed and the X gate can be implemented arbitrarily fast in principle.

To prepare the X-basis eigenstate $|SC_{r,\alpha'}^+\rangle$, we initialize the system into the vacuum state $|0\rangle$, and turn on the parity-preserving dissipation $\kappa_2 \mathcal{D}[\hat{S}(r)(\hat{a}^2 - \alpha'^2) \hat{S}^\dagger(r)]$. Since the parity is a conserved quantity, we obtain the even-parity state $|SC_{r,\alpha'}^+\rangle$ at a time $t \gg 1/4\kappa_2\alpha'^2$. We note that such a process is not protected from photon losses, since the dissipation does not correct the loss-induced stochastic phase flips. We will explore the implementation of more robust state preparation against losses in future work. One possible approach is to adiabatically inflate the SC from vacuum by tuning the dissipation (with an appropriate counter-adiabatic drive [4]), while maintaining the phase-flip correction.

To perform an X-basis measurement, we turn off the engineered dissipation and apply the standard QND bosonic parity measurement using a dispersive coupling between the bosonic mode and a transmon qubit [5–7]. A single photon loss during the dispersive coupling changes the parity and leads to stochastic measurement errors with a probability that depends on when the loss jump happens. As such, the loss-induced measurement error probability associated with such a single measurement is $p_m = \frac{1}{2} \bar{n} \kappa_1 T$. To suppress the loss-induced error, we apply the QND parity measurement three times and apply the parity-flipping dissipation to correct the loss after each measurement. Finally, we perform a majority vote to obtain the measurement outcome. Such a protocol leads to a loss-induced measurement error probability $p'_m = \frac{3}{2} \eta \kappa_1 \bar{n} T + \mathcal{O}((\kappa_1 T)^2)$, which maintains the η suppression factor against photon loss.

IV. DETAILS OF THE CONCATENATED QUANTUM ERROR CORRECTION

In this section, we present the details of the concatenated QEC with the SC qubits. The physical error rates of the SC that we use for Figs. 4(a)(c) are shown in Tab. I. We fix $\bar{n} = 4, \eta = 0.25$ ($r = 1.32$) for all the operations. The idling time depends on the specific location in a QEC cycle (idling during the ancilla readout and initialization,

idling during gate operations on other data qubits, etc.). We use the same state preparation time as in Ref. [2] to make sure that the leakage is below 10^{-3} . We assume that the X-basis measurement has negligible contribution to the QEC cycle time, given that the swap between the ancilla mode and the readout mode can be implemented much faster than all the other operations [8, 9] and the time-consuming repeated parity measurements on the readout mode can be performed in parallel with the QEC cycle. Furthermore, we numerically observe that both the surface code and the repetition code have a high tolerance against ancilla measurement errors. Their logical error rates are almost unaffected for measurement errors up to 10^{-2} . So we neglect the Z error rates from \mathcal{M}_X as well.

Operation	Idling	$\mathcal{P}_{ +\rangle}$	\mathcal{M}_X	CX (rep code)	CX (surface code)
η	0.25	0.25	0.25	0.25	0.25
Gate time	T	$10 * \frac{1}{\kappa_2 \alpha'^2}$	≈ 0	$1/\kappa_2$	T^*
p_Z	$\kappa_1 \eta \bar{n} T$	$\frac{10 \bar{n}}{\alpha'^2} \frac{\kappa_1}{\kappa_2}$	≈ 0	$\approx (1 + \eta) \bar{n} \frac{\kappa_1}{\kappa_2}$	$0.44 \left(\frac{\kappa_1}{\kappa_2}\right)^{2/3}$
$p_{X,Y}$	≈ 0	0	0	$1.38 \frac{e^{-2\alpha'^2}}{\alpha'^2}$	/

TABLE I. For CX gates, repetition code and surface code assumes different constraints and regimes. For repetition code, it works under the long gate time regime, and for $\kappa_1/\kappa_2 \geq 10^{-3}$, the optimal gate time is numerically found to be limited by the constraint, i.e. $T = \frac{1}{\kappa_2}$. For surface code, the optimal gate time is obtained through first principle simulations, which we denote as T^* . All quantities that are neglected in the simulations are labelled as \approx . $p_{X,Y}$ denotes the total probability of all non-dephasing errors. $p_{X,Y}$ of the CX gate in the surface-code simulation is not used.

We use the same QEC circuits and decoders (minimum-weight-perfect-matching decoder) as those in Ref. [2] for both the thin surface code and the repetition code.

For surface code simulations, we presented the logical error rates varying with physical error rate ratio κ_1/κ_2 and threshold as a function of average photon number in κ_1/κ_2 in Fig.4 (a, b). We numerically obtain the optimal CX gate time for certain κ_1/κ_2 , assuming a fixed cooling time T_{cool} . When the total Z error is optimal, we observe that the Z-error components can be described by similar relations of $p_Z^{\text{opt}} \propto \left(\frac{\kappa_1}{\kappa_2}\right)^{2/3}$. With these expressions for each Z error component, we perform circuit level simulations with Stim [10] to obtain logical error rates and estimations of thresholds at varying physical error ratios. In Fig.4 (b), we also includes thresholds for conventional cat encoding [2], where the optimal Z error is independent of the physical error ratio.

The repetition code simulation we performe focuses on the logical error rates and the minimal logical errors achievable, as shown in Fig.4 (c, d). For the logical error rates, the simulations are similar to surface code ones. The difference arise in the minimal logical error simulations, where the long gate time constraint is imposed. The constraint is primarily imposed such that the non-dephasing error rate of the CX gate can be expressed as $p_{X,Y} \approx 5.57 \times \frac{e^{-2\alpha'^2}}{\alpha'^2} \frac{1}{\kappa_2 T}$. In this regime, the Z error is dominated by loss-induced error, which is linear in κ_1/κ_2 . The optimal gate time for ratios larger then $\sim 10^{-3}$, is limited by this constraint. Similarly, we included minimal error rates for cat encoding, with the non-dephasing error rate expression of CX gate and Z logical error rates of repetition code shown in Table 7 and Eq. (39) in Ref. [2].

V. PHYSICAL IMPLEMENTATIONS

As discussed in the first Methods subsection in the main text, the desired nonlinear dissipator $\mathcal{D}[\hat{F}]$ with $\hat{F} \propto \hat{Z}_L \hat{S}(r) (\hat{a}^2 - \alpha'^2) \hat{S}^\dagger(r)$ can be realized via two distinct approaches, each involving nonlinear interactions that are more compatible with circuit QED systems, or trapped ion systems, respectively. Below, we provide more details for the relevant physical implementations.

A. Implementation in superconducting circuit systems: derivations of adiabatic elimination and error analysis

Recall in the main text, we consider physical implementation via two auxiliary modes b and c , so that the total system dynamics can be described by the following master equation

$$\frac{d}{dt} \hat{\rho} = -i \left[\frac{\lambda}{2} \hat{Z}_L \hat{b}^\dagger \hat{b} + (J_{ab} \hat{a}^\dagger \hat{b} + (J_{ac} \hat{a} - i J_{bc} \hat{b}) \hat{c}^\dagger + h.c.), \hat{\rho} \right] + \kappa_c \mathcal{D}[\hat{c}], \quad (2)$$

where the corresponding tunnel coupling rates are given by

$$J_{ab} = \sqrt{\Gamma_a \Gamma_b}/2, \quad J_{ac} = \sqrt{\Gamma_a \kappa_c}/2, \quad J_{bc} = \sqrt{\Gamma_b \kappa_c}/2. \quad (3)$$

We are interested in the regime where modes b and c effectively serve as a Markovian reservoir for the composite system consisting of logical qubit and the gauge mode degrees of freedom. In what follows, we first show how the desired system dissipator emerges following a standard adiabatic elimination procedure (e.g. see Ref. [11]) and assuming the relevant parameters are chosen such that the adiabatic approximation is valid. We then exactly solve the steady state dynamics of Eq. (2) under initial state with a single excitation in the gauge mode, and use that analytical solution to quantitatively derive the conditions on the physical parameters to be in the adiabatic regime, as well as the dominating error rate introduced by Eq. (2).

Following the convention in Ref. [11], we identify the ground and excited manifolds as the joint vacuum, and the excited state subspace of auxiliary modes b and c , respectively. We can thus separate the total system dynamics in Eq. (2) into contributions describing the ground (excited) state Hamiltonian \hat{H}_g (\hat{H}_e), the perturbative excitation (relaxation) coupling operator \hat{V}_+ (\hat{V}_-), as well as the decay jump operator \hat{L}_{loss} as

$$\hat{H}_g = 0, \quad \hat{H}_e = \frac{\lambda}{2} \hat{Z}_L \hat{b}^\dagger \hat{b} + i \frac{\sqrt{\Gamma_b \kappa_c}}{2} (\hat{b}^\dagger \hat{c} - \hat{c}^\dagger \hat{b}), \quad (4)$$

$$\hat{V}_- = \hat{V}_+^\dagger = \frac{\sqrt{\Gamma_a}}{2} \hat{a}^\dagger \left(\sqrt{\Gamma_b} \hat{b} + \sqrt{\kappa_c} \hat{c} \right), \quad \hat{L}_{\text{loss}} = \sqrt{\kappa_c} \hat{c}. \quad (5)$$

Note that the dissipation in Eq. (2) only involves a relaxation process from the excited to the ground manifold, we can directly apply the general formulas in [11] to adiabatically eliminate the auxiliary modes and obtain an effective quantum master equation involving \hat{Z}_L and \hat{a} . More specifically, the effective non-Hermitian Hamiltonian governing subspace with a single excitation in modes b or c can be written as

$$\hat{H}_{\text{NH}} = \hat{H}_e - \frac{i}{2} \hat{L}_{\text{loss}}^\dagger \hat{L}_{\text{loss}} \quad (6)$$

$$= \frac{\lambda}{2} \hat{Z}_L |1_b\rangle\langle 1_b| + i \frac{\sqrt{\Gamma_b \kappa_c}}{2} (|1_b\rangle\langle 1_c| - h.c.) - i \frac{\kappa_c}{2} |1_c\rangle\langle 1_c|, \quad (7)$$

so that we obtain the effective ground-state manifold system Hamiltonian \hat{H}_{eff} , and the jump operator \hat{L}_{eff} as

$$\hat{H}_{\text{eff}} = \hat{H}_g - \frac{1}{2} \hat{V}_- \left[\hat{H}_{\text{NH}}^{-1} + (\hat{H}_{\text{NH}}^{-1})^\dagger \right] \hat{V}_+^\dagger = 0, \quad (8)$$

$$\hat{L}_{\text{eff}} = \hat{L}_{\text{loss}} \hat{H}_{\text{NH}}^{-1} \hat{V}_+ = i \sqrt{\Gamma_a} \hat{a} \frac{i \lambda \hat{Z}_L - \Gamma_b}{i \lambda \hat{Z}_L + \Gamma_b}. \quad (9)$$

We have thus derived Eq. (18) in the main text.

For the purpose of analyzing the dominating error due to finite decay rate κ_c of the auxiliary reservoir mode c , we now view the logical qubit operator \hat{Z}_L as a qubit Pauli operator, and the gauge mode operator \hat{a} as the lowering operator of a genuine bosonic mode. We note that this treatment is valid in the relevant parameter regime we are interested in. In such case, we can derive exactly the long-time evolution of a generic initial state with a single excitation in the gauge mode \hat{a} and vacuum in the auxiliary modes b and c , which can be fully captured by the coherence function $\hat{\Sigma}_{L-}$ (i.e. off-diagonal density matrix element with respect to eigenbasis of \hat{Z}_L), as

$$\lim_{t \rightarrow \infty} \frac{\langle \hat{\Sigma}_{L-}(t) \rangle}{\langle \hat{\Sigma}_{L-}(0) \rangle} = \left(\frac{\Gamma_b - i\lambda}{\Gamma_b + i\lambda} \right)^2 \frac{1 + \frac{\Gamma_a \kappa_c (\Gamma_b + i\lambda)}{(\kappa_c + i\lambda)(\Gamma_b - i\lambda)^2}}{1 + \frac{\Gamma_a (\kappa_c^2 + i\Gamma_b \lambda)}{\kappa_c (\kappa_c + i\lambda)(\Gamma_b + i\lambda)}}. \quad (10)$$

To realize our desired dissipator, we set $\Gamma_b = \lambda$. From Eq. (10), it is straightforward to see that the conditions for validity of adiabatic elimination can be written as

$$\sqrt{\Gamma_a \Gamma_b} \ll \kappa_c, \quad \Gamma_a \ll \Gamma_b, \quad \Gamma_a \ll \kappa_c. \quad (11)$$

It is interesting to note that the adiabatic elimination does not require the two reservoir modes' decay rates to satisfy a hierarchy, i.e. $\Gamma_b \ll \kappa_c$. This might seem surprising at the first glance, as we motivate Eq. (2) based on the intuition that mode c is lossy and enables a directional coupling from a to b . However, from the perspective of doing adiabatic approximation, we only need to ensure that the excitation exchange between system (logical qubit and gauge mode) and the auxiliary modes is much slower than the internal reservoir dynamics of b and c , which also leads to Eq. (11).

In current superconducting circuit implementations, one of the relevant factors limiting the strength Γ_a of effective dissipation is the finite bandwidth of the auxiliary reservoir κ_c . For convenience, we now rewrite Eq. (11) as follows

$$\Gamma_a \ll \min\{\Gamma_b, \kappa_c, \kappa_c^2/\Gamma_b\}. \quad (12)$$

One can thus show that for a fixed value of κ_c , the optimal choice of Γ_b to maximize the effective dissipation strength Γ_a is $\Gamma_b = \kappa_c$, in which case we further have $\kappa_c = \Gamma_b = \lambda$. Substituting this expression into Eq. (10), we can in turn derive the leading-order error rate to the logical qubit coherence function as

$$\lim_{t \rightarrow \infty} \frac{\langle \hat{\Sigma}_{L-}(t) \rangle}{\langle \hat{\Sigma}_{L-}(0) \rangle} \simeq \left(\frac{\Gamma_b - i\lambda}{\Gamma_b + i\lambda} \right)^2 \left(1 - \frac{\Gamma_a}{2\Gamma_b} \right). \quad (13)$$

We thus recover the relation between ideal Z-error rate assuming a perfect dissipator $\mathcal{D}[\hat{F}]$, versus the simulated error rate via the discussed physical implementation, as $\eta_{\text{sim}} - \eta_{\text{pred}} = (1 - \eta_{\text{pred}})(\Gamma_a/2\Gamma_b)$.

B. Implementation in trapped-ion system

Fig. 6 in the main text describes the level scheme and laser configurations to the coupling Hamiltonians to implement the SC in trapped-ion systems. The setup involves the motional mode of the ion with Fock states $|n\rangle$ which is coupled to three internal states labeled $|g\rangle$, $|e\rangle$, $|f\rangle$. Starting from the atomic ground state $|g\rangle$, the system goes through a two-step coherent transition $|g\rangle \rightarrow |f\rangle \rightarrow |e\rangle$ with relevant driving lasers indicated in Fig. 6 by black and green arrows, respectively. In the first step, a laser drives the atomic transition $|g\rangle \otimes |n\rangle \rightarrow |f\rangle \otimes |n\rangle$ and the frequency-resolved second motional sidebands $|g\rangle \otimes |n\rangle \rightarrow |f\rangle \otimes |n \pm 2\rangle$, while the second step couples coherently $|f\rangle \otimes |n\rangle \rightarrow |e\rangle \otimes |n \pm 1\rangle$. Finally, state $|e\rangle$ is assumed to decay back to the ground state $|g\rangle$ via spontaneous emission. The effective dissipator acting on the motional state is obtained via adiabatic elimination of states $|e\rangle, |f\rangle$. Here we present the technical details of such a protocol.

Neglecting the momentum kicks first, the system dynamics is described by:

$$\begin{aligned} \frac{d}{dt} \hat{\rho} &= -i[\hat{H}, \hat{\rho}] + \Gamma \mathcal{D}[|g\rangle\langle e|] \hat{\rho} \\ \hat{H} &= \Omega_0(|f\rangle\langle g| + |g\rangle\langle f|) + \sum_{i=1}^3 \frac{1}{2} \Omega_i \cos[\eta_0(\hat{a}e^{-i\nu t} + \hat{a}^\dagger e^{i\nu t})] (|f\rangle\langle g|e^{-i\delta_i t} + |g\rangle\langle f|e^{i\delta_i t}) \\ &\quad + \sum_{i=4}^5 \frac{1}{2} \Omega_i \sin[\eta_0(\hat{a}e^{-i\nu t} + \hat{a}^\dagger e^{i\nu t})] (|e\rangle\langle f|e^{-i\delta_i t} + |f\rangle\langle e|e^{i\delta_i t}) \end{aligned} \quad (14)$$

By choosing $\delta_1 = -2\nu, \delta_2 = 2\nu, \delta_3 = 0, \delta_4 = -\nu, \delta_5 = \nu$ and neglecting the fast-rotating terms, we obtain:

$$\hat{H} = [\epsilon_1 \hat{a}^2 + \epsilon_2 \hat{a}^{\dagger 2} + \epsilon_3 (\hat{a}^\dagger \hat{a} + \hat{a} \hat{a}^\dagger) + \epsilon_0] |f\rangle\langle g| + (\epsilon_4 \hat{a} + \epsilon_5 \hat{a}^\dagger) |e\rangle\langle f| + h.c., \quad (15)$$

where $\epsilon_1 = -\frac{1}{4}\eta_0^2\Omega_1, \epsilon_2 = -\frac{1}{4}\eta_0^2\Omega_2, \epsilon_3 = -\frac{1}{4}\eta_0^2\Omega_3, \epsilon_0 = \frac{1}{2}(\Omega_0 + \Omega_3), \epsilon_4 = \frac{1}{2}\eta_0\Omega_4, \epsilon_5 = \frac{1}{2}\eta_0\Omega_5$. By setting $\epsilon_1 = \cosh^2 r \Omega'_{gf}, \epsilon_2 = \sinh^2 r \Omega'_{gf}, \epsilon_3 = \sinh r \cosh r \Omega'_{gf}, \epsilon_0 = -\alpha'^2 \Omega'_{gf}, \epsilon_4 = \frac{\cosh r}{\alpha'} \Omega'_{ef}, \epsilon_5 = \frac{\sinh r}{\alpha'} \Omega'_{ef}$, we obtain

$$\hat{H} = \Omega'_{gf} [\hat{S}(r)(\hat{a}^2 - \alpha'^2) \hat{S}^\dagger(r)] |f\rangle\langle g| + \Omega'_{ef} \frac{1}{\alpha'} \hat{S}(r) \hat{a} \hat{S}^\dagger(r) |e\rangle\langle f| + h.c. \quad (16)$$

In the adiabatic regime $2\alpha'\Omega'_{gf} \ll \Gamma, \Omega'_{gf} \ll \Omega'_{ef}$, we can obtain a reduced dynamics on the motional mode by adiabatically eliminating the $|e\rangle, |f\rangle$ states:

$$\frac{d}{dt} \hat{\rho}_m = \kappa_2 \mathcal{D}[\hat{F}] \hat{\rho}_m, \quad (17)$$

where $\kappa_2 = (\frac{\Omega'_{gf}}{\Omega'_{ef}})^2 \Gamma$. Numerically we find that we can obtain the dissipator \hat{F} with the desired rate by setting $\Omega'_{ef} = 0.5\Gamma, \Omega'_{gf}/\Omega'_{ef} = 1/20$. The leading-order off-resonant term of \hat{H} is $\frac{1}{2}(\Omega_1 e^{2i\nu t} + \Omega_2 e^{-2i\nu t}) |f\rangle\langle g| + h.c.$, which leads to AC stark shift of the gf transition frequency. One can compensate this term by adjusting the laser detuning w.r.t ω_f , or add a compensation drive to the bare gf transition. We can provide a rough estimate of the achievable engineered dissipation strength κ_2 based on attainable experimental parameters $\nu = 30$ MHz, $\eta_0 = 0.15$ [12]. With

the leading-order off-resonant term compensated, we can obtain a good stabilization for a Γ up to 200 KHz, which leads to $\kappa_2 = 0.5$ KHz. This estimated rate is much larger than the typical ambient noise rates of the ions, which are in the level of 10 Hz [13]. Note also that the prominent noise in many trapped-ion platforms was identified as the dephasing [13], which, compared to the loss errors, can be better suppressed by the SC.

We give a brief analysis on the effect of the momentum kicks. In the Lamb-Dick regime ($\eta_0 \ll 1$), the system dynamics that include the leading-order contribution from the momentum kicks read:

$$\frac{d}{dt}\hat{\rho} = -i[\hat{H}, \hat{\rho}] + \Gamma\mathcal{D}[|g\rangle\langle e||\hat{\rho}] + \left(\Gamma\eta_0^2 \int_{-1}^1 u^2 N(u) du\right) \mathcal{D}[\hat{a} + \hat{a}^\dagger] |g\rangle\langle e|\hat{\rho}|e\rangle\langle g|. \quad (18)$$

We can see that the third term, which results from the momentum kicks, leads to extra phase flips of the SC when the ion decays from $|e\rangle$ to $|g\rangle$. As such, the third term competes with the second term when correcting the errors on the motional mode that induce the internal-state transition cycle $|g\rangle \rightarrow |f\rangle \rightarrow |e\rangle \rightarrow |g\rangle$. Fortunately, the rate of the third term is suppressed by η_0^2 . So the momentum kicks only lead to a small increase of the phase-flip suppression factor $\eta \rightarrow \eta + \mathcal{O}(\eta_0^2)$.

In the end, we present a candidate trapped-ion platform suitable for our scheme. Note that we require resolved sideband conditions, i.e. the decay rate of $|e\rangle$ is assumed smaller than the trap frequency. Such a tunable engineered effective spontaneous transition rate can be engineered via Raman processes as optical pumping (see below).

The prototypical level scheme for trapped ion is reviewed in Ref. [14] in context of implementation of trapped-ion quantum computing for the case of $^{40}\text{Ca}^+$ ions. We now briefly describe the mapping of our level scheme $|g\rangle, |e\rangle, |f\rangle$ and laser configuration to levels of the Ca^+ ion, as available in these experiment. $^{40}\text{Ca}^+$ has an electronic ground state $^2S_{1/2}$ coupled via a quadrupole transition to metastable excited states $^2D_{5/2,3/2}$, and both the ground and metastable states can excite the short-lived $^2P_{3/2,1/2}$ states in dipole-allowed transitions (see Fig. 1 of Ref. [14]).

A first mapping is obtained by identifying $|g\rangle, |e\rangle, |f\rangle$ with long-lived states $^2S_{1/2}, ^2D_{5/2}$, and $^2D_{3/2}$, respectively, where the first transition (black arrows in Fig. 6 main text) corresponds to the quadrupole transition, while the second step (green arrows in Fig. 6 main text) can be implemented as a Raman transition coupling the two metastable D -states. A tunable effective decay rate back to the S -ground state can be obtained as an optical pumping process via the short-lived P states.

A second mapping identifies the two Zeeman ground states $|^2S_{1/2} m = \pm 1/2\rangle$ with levels $|g\rangle, |f\rangle$ and drives the second order sidebands, as familiar from sideband cooling utilizing Raman cooling via intermediate P -states (see Fig. 2d in Ref. [14]). The second coherent step can then be implemented via transitions to D -states, followed by engineered decay via short-lived P -states.

-
- [1] G. Pantaleoni, B. Q. Baragiola, and N. C. Menicucci, *Physical Review Letters* **125**, 040501 (2020).
 - [2] C. Chamberland, K. Noh, P. Arrangoiz-Arriola, E. T. Campbell, C. T. Hann, J. Iverson, H. Putterman, T. C. Bohdanowicz, S. T. Flammia, A. Keller, *et al.*, *PRX Quantum* **3**, 010329 (2022).
 - [3] S. Puri, L. St-Jean, J. A. Gross, A. Grimm, N. E. Frattini, P. S. Iyer, A. Krishna, S. Touzard, L. Jiang, A. Blais, *et al.*, *Science advances* **6**, eaay5901 (2020).
 - [4] S. Puri, S. Boutin, and A. Blais, *npj Quantum Information* **3**, 1 (2017).
 - [5] L. Sun, A. Petrenko, Z. Leghtas, B. Vlastakis, G. Kirchmair, K. Sliwa, A. Narla, M. Hatridge, S. Shankar, J. Blumoff, *et al.*, *Nature* **511**, 444 (2014).
 - [6] C. T. Hann, S. S. Elder, C. S. Wang, K. Chou, R. J. Schoelkopf, and L. Jiang, *Physical Review A* **98**, 022305 (2018).
 - [7] S. S. Elder, C. S. Wang, P. Reinhold, C. T. Hann, K. S. Chou, B. J. Lester, S. Rosenblum, L. Frunzio, L. Jiang, and R. J. Schoelkopf, *Physical Review X* **10**, 011001 (2020).
 - [8] S. de Graaf, B. Chapman, J. Curtis, Y. Zhang, N. Frattini, M. Devoret, S. Girvin, and R. Schoelkopf, *Bulletin of the American Physical Society* (2022).
 - [9] A. Maiti, Y. Lu, S. Ganjam, J. Garmon, Y. Zhang, S. Girvin, L. Frunzio, and R. Schoelkopf, *Bulletin of the American Physical Society* (2022).
 - [10] C. Gidney, *Quantum* **5**, 497 (2021).
 - [11] F. Reiter and A. S. Sørensen, *Physical Review A* **85**, 032111 (2012).
 - [12] C. Monroe, D. Meekhof, B. King, and D. J. Wineland, *Science* **272**, 1131 (1996).
 - [13] C. Flühmann, T. L. Nguyen, M. Marinelli, V. Negnevitsky, K. Mehta, and J. Home, *Nature* **566**, 513 (2019).
 - [14] P. Schindler, D. Nigg, T. Monz, J. T. Barreiro, E. Martinez, S. X. Wang, S. Quint, M. F. Brandl, V. Nebendahl, C. F. Roos, M. Chwalla, M. Hennrich, and R. Blatt, *New Journal of Physics* **15**, 123012 (2013).